Lattice-Boltzmann accuracy in pore-scale flow simulation

R.S. Maier *, R.S. Bernard

US Army Engineer Research and Development Center, 3909 Halls Ferry Rd., Vicksburg, MS 39180, United States

ABSTRACT

We investigate the possibility of using nominally second-order-accurate techniques for resolving flow about solid boundaries as a means of improving accuracy and reducing grid resolution requirements in pore-scale simulations. An LBGK method is used to calculate flow in several geometries of increasing complexity, using a first-order accurate and two nominally second-order-accurate methods for no-slip boundaries. The geometries include uniform flow past an isolated sphere, quadratic flow past a sphere near a wall, flow through a BCC array of spheres, and through a randomly packed bed of spheres. The packed bed flows are also used to compare hydrodynamic dispersion results. The results confirm second-order-accurate behavior where Navier–Stokes flows are clearly developed. However 3D pore-scale simulations involve a trade-off between resolution of the flow and the number of pore spaces, and there is a resolution threshold, below which certain flow features, such as recirculation, are not resolved. We conjecture that most simulations will tend to operate near this threshold because of the competing demands for resolution and statistical accuracy. We consider local flow features and the velocity distribution, in addition to hydraulic permeability and drag, to provide a fuller understanding of accuracy near this threshold.

Published by Elsevier Inc.

1. Introduction

Pore-scale simulations may be used to characterize macroscopic properties of a porous medium, such as permeability, drag, or dispersivity, by simulating fluid flow and transport in a sample and averaging the properties from ensemble statistics. They also have great potential for the simulation of dynamic phenomena that depend on accurate resolution of near-surface flows. Pore-scale simulations must have sufficient accuracy in the pore spaces as well as a sufficiently large sample of the porous media. These two requirements represent a trade-off in terms of computational resources. In the present work we are primarily concerned with simulation accuracy in a single realization, and not with the statistical accuracy of the ensemble averages. There is a substantial literature on the statistical characterization of porous media in the soils and geophysics community. Early pore-scale modeling results on this topic were presented by Zhang et al. [1] in the context of fluid permeability and Hazlett [2] in the case of two-phase flows.

Accuracy in pore-scale simulations is a function of the grid resolution and the efficiency of the numerical method in reducing error as a function of the grid parameter, h. Here we assume a regular grid, and h is the dimension of a cubic grid cell. In many practical cases, the grid resolution is determined by a 3D digital image of a porous medium, but grid resolution is often a choice; for example, experiments that use packed beads can be simulated by generating 3D random sphere packings. The appropriate resolution can be informed by a grid convergence study, where a simulation is solved at several levels

of resolution to determine the sensitivity of the solution to h. Doubling h on a regular grid reduces the number of grid points and the corresponding computational effort by nearly an order of magnitude, and this motivates improvements in accuracy to reduce grid resolution requirements.

In the present work we are concerned with the lattice-Boltzmann method for viscous fluid flow and associated techniques for modeling boundary conditions. The LB method is based on a kinetic model of dilute-gas hydrodynamics and would therefore seem an unlikely choice for incompressible flows in porous media. The method recovers Navier–Stokes behavior in the low Mach number limit, which is a common regime in pore-scale flow, and by a comparatively simple numerical algorithm, which, although not necessarily less complex than an explicit Stokes flow solver, can be implemented by a first-year graduate student in the course of a day or two. This simplicity has as much to do with the use of a regular grid and an explicit time step, as with any intrinsic simplicity of the governing equations. Claims of exceptional computational parallelism similarly have more to do with the ease of implementation on parallel architectures than with any special properties of the algorithm. In fact, the method has a high ratio of memory reference to computation, which does not favor an especially high parallel efficiency, which is also true of other approaches to solving the Navier–Stokes equations on a regular grid with an explicit time step.

The LB method is known to be second-order-accurate in a bulk, or interior, flow away from boundaries, similar to what can be expected from a standard finite-difference implementation of the Navier–Stokes equations [10]. In applications to pore-scale flow, the boundary techniques take on particular importance, as they may either support or degrade the accuracy of the LB method.

The study of boundary techniques has been a significant theme in the literature. The earliest treatments analyzed the accuracy of the bounce back technique [13–15,18], an especially simple implementation of the no-flow boundary condition, and showed the technique supports second-order accuracy only under certain conditions. Later treatments proposed a variety of interpolation techniques designed to support second-order accuracy [16,17,20,19,21]. Mei et al. [22] were perhaps the first to examine the grid convergence of an interpolation technique in a systematic fashion on a set of representative test problems of moderate complexity. There have been relatively few treatments of boundary-fitted coordinates and curvilinear grids [23–25], or volume-of-fluid approaches [26,27]. Such approaches are already well-developed for the solution of the Navier–Stokes equations.

There have been several comparative treatments of interpolation boundary techniques, from a theoretical perspective [28], and from a computational point of view [29–31]. Junk and Yang's analysis unifies our understanding of several interpolation techniques as corrections to the bounce back technique. These treatments have tended to convey the impression that interpolation techniques support second-order accuracy in channel flows and certain integral measures, such as hydraulic permeability. They also demonstrate that some boundary techniques, such as multi-reflection [32] can deliver a lower magnitude of error than others by making greater use of local velocities at neighboring nodes. However, a careful examination of these results suggests the convergence behavior depends on the particular problem, depends on the LB parameter settings, is irregular over the range of h, and is something less than second-order for a number of interpolation methods applied to problems of moderate to high complexity. Indeed, for certain parameter settings, the behavior is not substantially different from that of the bounce back technique.

Bond et al. note that some boundary techniques in many CFD codes with second-order interior schemes should be expected to generate first-order error. "Whether or not this error remains local to the boundary or propagates into the interior depends upon the mathematical character at the boundary." They further note, "If first-order error is generated locally at a boundary and does not propagate into the domain, then it is possible for the L1 or L2 norms of the error to show second-order convergence when the error calculation is performed over the entire domain." [33–35].

From a practical view point, something less than second-order accuracy is quite acceptable. At the same time, second-order behavior of one measure for one class of problems does not guarantee the same for another measure and class of problems. For example, a measure that depends on resolving secondary flow features may not converge as quickly as one that only depends on the average flux.

In the present work we consider two interpolation techniques in relationship to the bounce back technique. One interpolation technique is widely accepted and comparatively simple to implement. The other is novel and to our knowledge untested on practical problems. These are considered to be representative of the interpolation approach, although not necessarily the most accurate or robust in any specific application. We apply these techniques to a sequence of 3D problems of increasing complexity that illustrate features of porous media flow, culminating with flow through a random array of close-packed spheres. Our interest is in the extent to which the different techniques support the accuracy of the LB method, and to a lesser extent on the robustness of the LB method. Hence, we make no effort to average the results over different grid orientations or LB parameters.

An important consideration often unstated in discussions of interpolation techniques is the requirement to establish interpolation points representing the boundaries. On a regular grid, this requires the calculation of distances between grid points and boundary surfaces, and is a significant computational task, even with an analytical description of the boundaries such as a list of sphere coordinates. In many cases, pore-structure images obtained from SEM or NMR have a resolution adequate for flow simulation, and the question is whether to apply smoothing algorithms to the pore geometry in order to use interpolation techniques, or whether to simply employ the conventional practice of coloring grid cells as solid or void, i.e. the "stair-step" representation. On this question, the last section of this work should be of interest because it evaluates the sensitivity of transport to the use of stair-step versus smooth boundaries.

1.1. LBGK method

The discrete-velocity Boltzmann equation for the distribution of a particle in a fluid is given by

$$\frac{\partial f_i}{\partial t} + e_i \cdot \nabla f_i = C(\mathbf{f}),$$

where $e_i, i = 1, \ldots, N_e$, are the direction vectors representing the discrete-velocity space, and $\mathbf{f} = \{f_i, i = 1, \ldots, N_e\}$ is the discretization of the particle mass distribution in velocity space, and C denotes a collision operator acting on $\mathbf{f}$. By definition, the particle mass density and momenta are recovered from the first and second moments of $\mathbf{f}$, i.e., $\rho = \sum f_i$ and $\rho v = \sum f_i e_i$.

The lattice-Boltzmann method may be generally described as a Lagrangian finite-difference method for the simulation of the discrete-velocity Boltzmann equation [11]. The term Lagrangian refers to the idea that the convective derivative is solved separately from the collision operator by propagating mass along the characteristic lattice vectors. In the present work, we use a cubic lattice with a 19-vector model (d3q19) of velocity space ($N_e = 19$), and the single relaxation time collision operator (BGK),

$$f_i^C(x, t) = f_i(x, t) - \frac{1}{\tau}(f_i(x, t) - f_i^{EQ}(x, t)) \tag{1}$$

$$f_i(x + e_i, t + 1) \;\leftarrow\; f_i^C(x, t) \tag{2}$$

where $f_i^{EQ} = \rho(A + Be_i \cdot v + C(e_i \cdot v)^2 + Dv \cdot v)$ is the customary form of the equilibrium distribution function. The coefficients of f_i^{EQ} are derived under a set of assumptions and a procedure that allow the method to recover Navier–Stokes behavior in the low Mach number limit [12]. The derivation also yields expressions for the kinematic viscosity $v = (2\tau - 1)/6$ and sound speed $c_s = \sqrt{1/3}$. Upon choosing the lattice grid spacing, h, these expressions may be used to establish the conversion between lattice and physical units. For economy and simplicity we take τ equal to unity. At each time step, the f_i relax to their equilibrium values before propagating to adjacent lattice sites. This permits the calculation simply in terms of ρ and v without storing the f_i. The advantage is gained, however, at the expense of some flexibility, because the relaxation parameter can otherwise be used to decrease the viscosity, allowing the simulation of a wider Reynolds number range for a given lattice spacing, h.

Our restriction of τ may leave an incomplete picture of the error. Error in the LBGK method is related not only to the Mach number, but also to the Knudsen number. The Knudsen number, Kn, is the ratio of the mean free path to the relevant length scale for momentum transport, here given by $Kn = (2\tau - 1)/(L/h)$, where L/h is the length in units of lattice grid spacing and $2\tau - 1$ approximates the mean free path. Analysis of the LBGK method by Reider and Sterling [10] reveals distinct error terms of $O(Kn^2)$ and $O(M^3)$. Thus, error depends on the relaxation parameter, τ, as well as the grid spacing parameter, h.

A number of authors have noted the dependence of permeability error on τ for a given value of h or M. Ginzbourg and D'Humieres observed a dependence for various geometries, including random fibers and a cubic array of spheres [32]. Pan et al. presented the dependence in greater detail for random spheres and a BCC array of spheres [31]. Chun and Ladd studied the dependence for the multiple-relaxation-time lattice-Boltzmann method for simple cubic and BCC arrays of spheres [30].

The joint dependence of error on Kn and M can be observed in the simple case of flow through a square duct. For second-order-accurate boundary conditions, we found neither the Mach number nor the Knudsen number separately to be a very good index for error with the duct flow problem [3]. On the other hand, the product of the Mach and Knudsen numbers is a fairly good index for relative error, as shown by Fig. 1(a), which plots maximum relative error versus KnM for 206 separate square duct simulations. In all simulations, the d3q15 velocity-space discretization was used with periodic inflow and
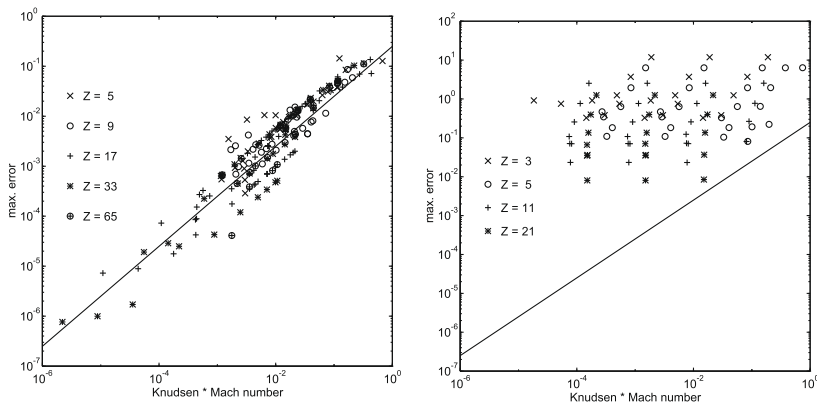

Fig. 1. Maximum error versus KnM for duct flow: (left) second-order-accurate boundary conditions, and (right) first-order-accurate boundary conditions.

outflow conditions, and a uniform body force to drive the flow. The no-slip condition was implemented by a second-order-accurate method [18]. The simulation parameters vary over the ranges, $5/8 \leqslant \tau \leqslant 8, 4 \leqslant L \leqslant 64$, and $10^{-3} \leqslant M \leqslant 0.6$.

The predictive value of the error index, KnM, apparently depends on second-order spatial convergence in both the LBM and the boundary method. If a first-order-accurate method is used for the no-slip boundaries, the relative error is not well-correlated with KnM, as shown in Fig. 1(b), which plots maximum relative error versus KnM where bounceback is the prescribed boundary condition. In this case, the maximum relative error occurs near the boundaries.

We also caution that our use of the LBGK d3q19 gives an incomplete picture of how the lattice velocity-space discretization may influence error. For example, a number of authors have noted the robustness of d3q19 as compared to the d3q15 model [4,22] for fluid flows in porous media. The accuracy of different velocity-space discretizations remains an important question because LBGK has been extended to modeling several other transport processes in porous media, including heat transfer [5], species transport [6], and electrokinetic flows [7–9]. It is unclear whether the conclusions about stability and accuracy of the different discretizations for modeling fluid flow will also apply to these more recent developments.

1.2. Techniques for no-slip boundaries

Let Ω represent the fluid domain, and let $S = \{x_j | x_j \in \Omega, \exists x_j - e_i \notin \Omega\}$ define the set of lattice nodes, or grid points, adjacent to the boundary, such that at least one neighboring lattice node is not in the fluid. For each $x_j \in S$, the LB time step (1) and (2) depends on one or more undefined values, $f_i(x_j - e_i, t)$, that originate from the boundary. Hence the need for boundary techniques to define these values. For each $x_j \in S$, let $V_j = \{i | x_j - e_i \notin \Omega\}$ define the indices of the lattice vectors emerging from the boundary and let $x_j - q_{ji}e_i$ define the intersection of e_i with the boundary, where $0 < q_{ji} \leqslant 1$ (Fig. 2). If y_n is the normal distance between x_j and the boundary, then $y_n \leqslant |q_{ji}e_i|$.

Although the LB method is formally second-order-accurate in space [10],

$$\|v - v_h\|_\infty \leqslant 1/4 \|v - v_{2h}\|_\infty$$

the technique for computing boundary conditions may support or degrade the accuracy of the LB method. For example, the bounce back technique, given below for a stationary boundary,

$$f_i(x_j, t_{n+1}) = f_{\bar{i}}^b(x_j, t_n) = f_{\bar{i}}^C(x_j, t_n), \quad \bar{i} = \{i | e_i = -e_i\} \tag{3}$$

is known to be formally first-order-accurate for velocity [28]. Even though this technique has been found to support second-order accuracy for favorable alignments of the boundary and lattice, it is fairly easy to construct examples which degrade the accuracy of the flow solution. Junk and Yang show that a correction to the bounce back technique of the form

$$f_i(x_j, t_{n+1}) = f_{\bar{i}}^b(x_j, t_n) - h^2(2q_{ji} - 1)e_i \cdot \nabla f_i^{(1)} \tag{4}$$

may support second-order accuracy in the flow, where $f_i^{(1)}$ appears in the expansion

$$f_i(x, t) = f_i^{(0)}(x, t) + h f_i^{(1)}(x, t) + h^2 f_i^{(2)}(x, t) + \cdots$$
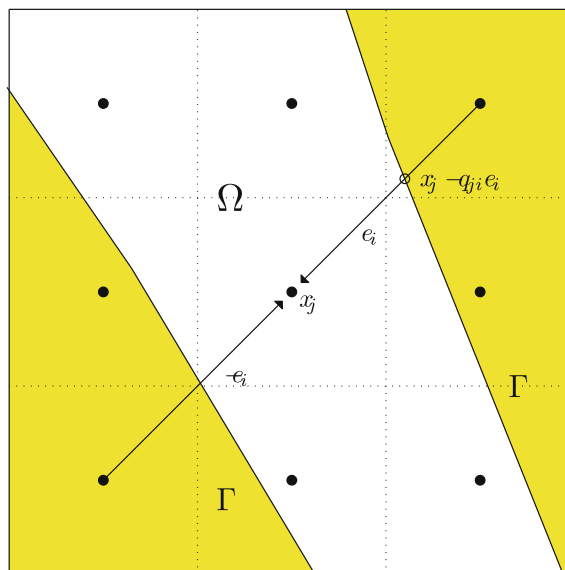

Fig. 2. Lattice nodes in fluid (Ω) and solid (Γ) regions.

Their asymptotic analysis shows that the directional derivative in (4) may be approximated as

$$-h^{-2}(f_i - f_i^C) = e_i \cdot \nabla f_i^{(1)} + O(h^3) \tag{5}$$

and they show that a number of existing interpolation techniques actually employ a correction of this form. The BFL technique [36] (Eq. (5), p. 3454) is an example of such a correction:

$$f_i(x_j, t_{n+1}) = \begin{cases} f_i^b(x_j, t_n) - (2q_{ji} - 1)[f_i^C(x_j - e_i, t_n) - f_i^C(x_j, t_n)] & q_{ji} < 1/2 \\ f_i^b(x_j, t_n) - (1/2q_{ji} - 1)[f_i(x_j, t_n) - f_i^C(x_j, t_n)] & q_{ji} \geqslant 1/2 \end{cases}$$

A difficulty arises when applying this correction to $f_i(x_j, t_{n+1})$ if both f_i and f_i originate from the boundary. In this case, it is not clear how to approximate $\nabla f_i^{(1)}$ from the available variables. A convenient but not completely satisfying procedure is to ignore the correction in these cases and use simple bounce back. As an alternative, Junk and Yang proposed a correction that averages the non-equilibrium contribution over all of the lattice vectors i originating from the boundary. We write their POP technique for our present implementation as

$$f_i(x_j, t_{n+1}) = f_i^b(x_j, t_n) + \sum_{k=1}^{N_e} K_{ik}[f_k(x_j, t_{n+1}) - f_k^C(x_j, t_n)], \quad i \in V_j \tag{6}$$

where the coefficients of the matrix K are defined as

$$K_{ik} = -\frac{9}{2}(1 - 2q_{ji})\omega_i((e_i \cdot e_k)^2 - \frac{1}{3}e_i \cdot e_i - e_{i\alpha}^2(e_k \cdot e_k - 1)) \tag{7}$$

The POP technique involves the solution of a small linear system at each grid point near the surface, where the number of unknown $f_i(x_j, t_{n+1})$, and hence the dimension of the system, is given by $|V_j|$.

1.3. Error measures

We are interested in the error near the no-slip surfaces, and in whether this error, which is associated with the boundary technique, supports or degrades the accuracy of the LB method. For those geometries for which there exists an exact solution, we can establish the accuracy of the LB method for that particular geometry by measuring convergence to the solution as the grid is refined. Otherwise, we measure the convergence to a computed solution obtained at high resolution, although this does not establish the order of accuracy because of the possibility of differences between the computed and true solutions.

If $\xi(h)$ denotes an error measure obtained with grid spacing h, we consider the power-law model $\xi(h) \propto h^\beta$, and estimate the order of convergence by a linear least-squares solution of

$$\log \xi(h) = \log \alpha + \beta \log h + \omega \tag{8}$$

The noise term, ω should be independent of h, but in some cases we observe clear departures from linearity that reveal issues in resolving the flow. The velocity errors associated with a second-order-accurate method should converge as $O(h^2)(\beta = 2)$ and those associated with a first-order method as $O(h)(\beta = 1)$.

Certain global error measures involve cumulative errors over a number of grid points, and because the grid density depends on h, their convergence behavior requires some comment. The normalized global L_2 norm,

$$L_2^\Omega = \frac{\sqrt{\sum_{x_j \in \Omega}|v_j - v_j^*|^2}}{\sqrt{\sum_{x_j \in \Omega}|v_j^*|^2}} \tag{9}$$

is expected to converge as $O(h^2)$ for a second-order-accurate method and as $O(h)$ for a first-order-accurate method. In either case, the denominator should converge as $O(h^{-3/2})$ because the number of grid points increases as $|\Omega(h)| \propto h^{-3}$ while the velocity remains essentially constant as the grid is refined. The numerator is expected to converge as $O(h^{1/2})$ for a second-order method, where $|v_j - v_j^*| \propto h^2$, and should converge as $O(h^{-\frac{1}{2}})$ for a first-order-accurate method.

The error associated with grid points near the surface is of particular interest, and the normalized surface L_2 norm,

$$L_2^S = \frac{\sqrt{\sum_{x_j \in S}|v_j - v_j^*|^2}}{\sqrt{\sum_{x_j \in S}|v_j^*|^2}} \tag{10}$$

is expected to converge as $O(h)$ if the boundary technique is second-order-accurate at the boundaries, and as $O(h^0)$ if the technique is first-order-accurate at the boundaries. In either case, the denominator should converge as $O(h^0)$ because the number of surface-adjacent grid points increases as $|S| \propto h^{-2}$ while the velocity at these grid points is expected to decrease as $v \propto h$.

2. Uniform flow past a sphere

Stokes flow past an isolated sphere allows the study of impinging flow, an important phenomena in porous media, without the complication of secondary flows. Pressure decreases monotonically between the forward to the rear stagnation points. The flow is otherwise unrestricted, so velocity perturbations fall off slowly, as $1/r$, with distance from the sphere. This is a classical problem with a well-known exact solution and many published numerical treatments of the departure from Stokes flow at higher Reynolds numbers. Here we mention only the previous work involving LB boundary techniques applied to this problem. Ladd [37] analyzed the error associated with LB simulations of flow past a sphere and we discuss his analysis of drag error below. Mei et al. [22] previously examined uniform flow over a sphere at $Re = 10$ using the LB method with a curved boundary technique derived from that of Filippova and Hanel [21]. Although an analytical solution is unavailable for this flow rate, they were able to study grid convergence over a small range of grid spacing, $3h < r < 4h$. They concluded that the far-field solution was well converged in this range. Our calculations confirm their results for the same parameter range.

A more careful examination of boundary techniques is possible in the creeping flow regime, and it is possible to exclude the influence of far-field boundary conditions, in order to isolate the effect of the no-slip boundary techniques. To exclude far-field boundary effects, we used the analytical solution as Dirichlet conditions on a spherical boundary of radius $10r$ containing the isolated sphere. Furthermore, we took the analytical solution as the initial condition everywhere. The convergence criterion for the calculation was

$$|(F^{t+1} - F^t)/F^t| < 10^{-6} \tag{11}$$

where F is the drag force defined below in Eq. (12) and the superscript denotes the time step. This statistic is an integral measure of the change in the solution at $x_j \in S$.

2.1. Velocity error at surface-adjacent grid points

The set S includes all grid points x_j adjacent to the sphere surface. The perpendicular distance between x_j and the surface is in the range $0 < y_n \leqslant \sqrt{3}h$, and for $x_j \in S$, we find that the velocity magnitude increases with distance, $|v^*| \propto y_n$ (Fig. 3(a)), where $v^* = v^*(x_j)$ denotes the analytical solution. The error magnitude, $|v - v^*|$ at these surface-adjacent grid points is essentially independent of y_n, but clearly depends on the boundary technique. For example, at a resolution of $r/h = 10$, the error associated with BFL is about twice that of POP, and the error associated with bounce back is about twice that of BFL (Fig. 3(b)). The (nondimensional) error is $L_2^S(h = 0.1r) = \{0.0139, 0.0270, 0.0641\}$ for POP, BFL, and BB, respectively.

2.2. Velocity error along the centerline

The sphere is centered at the origin and the direction of flow is aligned with the z-axis, or centerline. The centerline connects the upstream boundary to the forward stagnation point and the aft stagnation point to the downstream boundary. Fig. 4 shows the centerline error profile and illustrates how the error falls away with distance from the sphere. Note the error closest to the stagnation points is actually lowest with the bounce back technique for this particular grid alignment. This is not the general case but illustrates the relative performance of the boundary techniques at the surface depends on the problem and the grid. However, the error falls away faster with distance from the surface using the BFL and POP techniques, and this result is general for all values of h studied here.
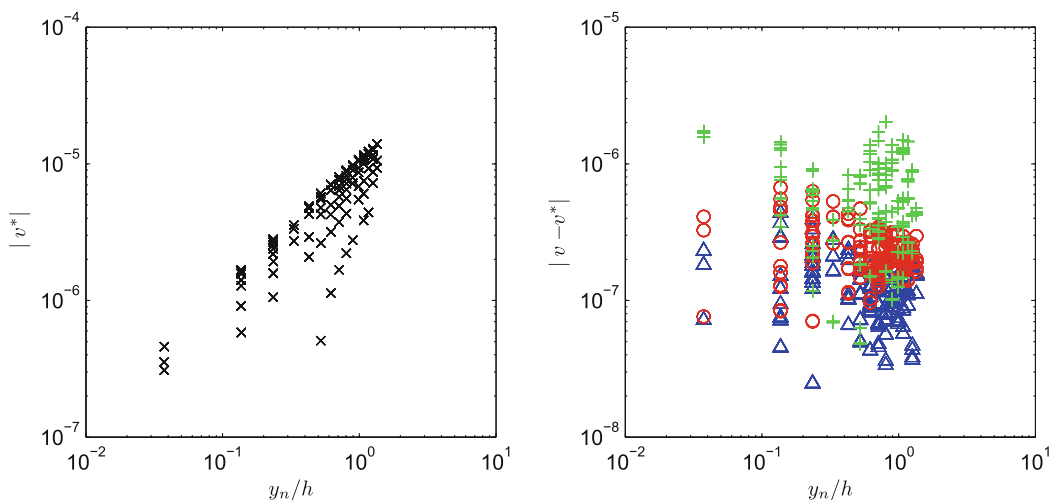

Fig. 3. Flow past an isolated sphere: velocity magnitude (left) and velocity error (right) at surface-adjacent grid points, $r/h = 10$. ○ = BFL, + = BB, △ = POP.
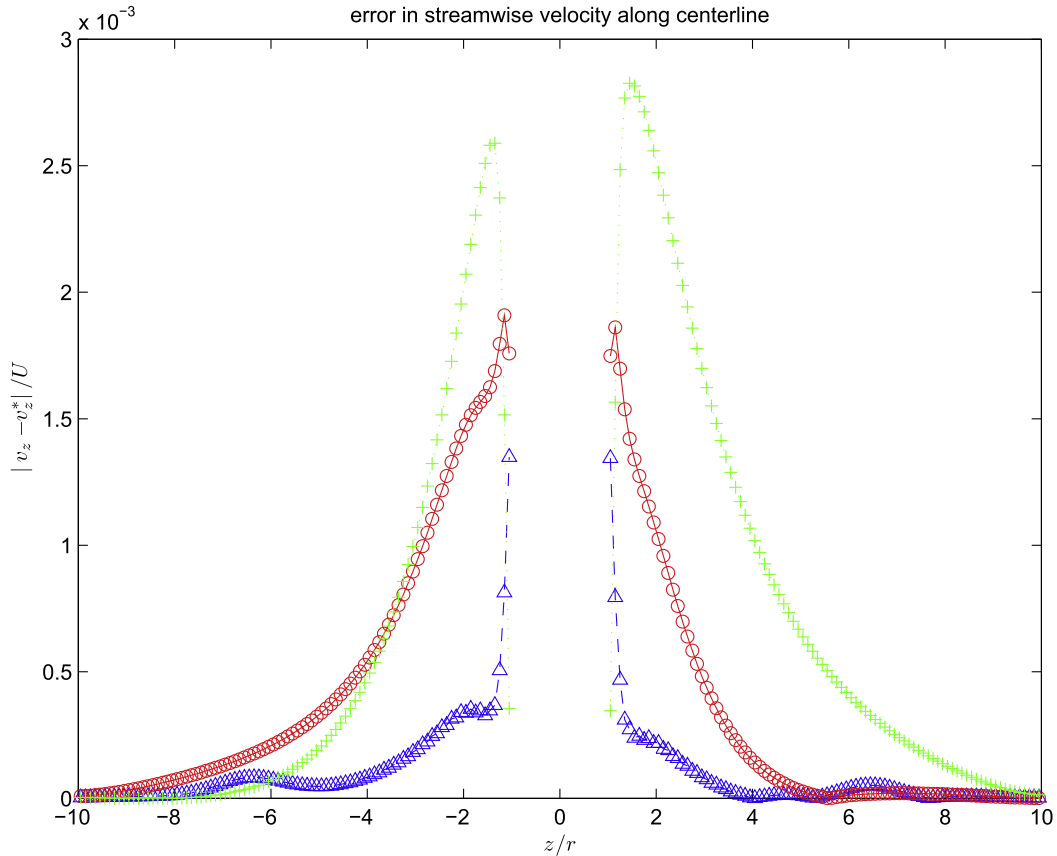
Fig. 4. Flow past an isolated sphere: relative error in streamwise (z) velocity along centerline. r/h = 10. The error is relative to U, the free-stream velocity. $\circ$ = BFL, + = BB, $\triangle$ = POP.

2.3. Accuracy of the boundary technique

In this section, convergence is evaluated for fixed stations, global measures, and surface measures. We chose two fixed stations, both at a distance of $1.5r$ from the sphere center, one along the centerline and the other on the transverse axis. On the coarse grid where $r = h$, these stations are only one half grid space from the surface, while at finer resolution these stations are not surface-adjacent grid points. For example, when $r/h = 10$, their distance from the surface is approximately $5h$. At these stations, the error for BFL is strictly decreasing and the error for POP and BB is non-monotonically decreasing (Fig. 5(a)). For $x = [0, 0, -1.5r]$, on the centerline, a linear least-squares fit of the relative error, $|(v_z - v_z^*)/v_z^*|$, to the power-law function (8) yields exponents $\beta = \{-1.78, -2.31, -1.03\}$ for the BFL, POP, and bounce back techniques, respectively. For $x = [0, -1.5r, 0]$, on the y-axis, $\beta = \{-2.01, -2.32, -1.34\}$. The pressure error, which is expected to converge as $O(h)$, actually converges as $O(h^2)$ for this problem, when calculated at the point $x = [0, 0, -1.5r]$. The LB method is expected to achieve second-order accuracy unless errors at the boundary propagate into the fluid, so error measures are expected to increase quadratically with h. By these measures, we conclude that BFL and POP support the theoretical accuracy of the LB method on interior flows, second-order in velocity and first-order in pressure, while the bounce back method supports only first-order accuracy in velocity.

The global error, L_2^{Ω}, is plotted against r/h in Fig. 5(b) and its convergence behavior confirms the results obtained at fixed stations in the flow. The error decreases monotonically, or nearly so, for BFL and POP, but shows some volatility with bounce back. The L_2^{Ω} error was fitted to (8) and the resulting power-law exponents are $\beta = 2.00$ for BFL and $\beta = 2.11$ for POP. These values are consistent with a second-order-accurate method (see Section 1.3). The exponent for bounce back is $\beta = 1.35$, reflecting something between first and second-order accuracy. The global maximum norm was also computed, but does not clearly support the previous results. A least-squares fit of the maximum error, L_{∞}^{Ω}, to (8) yields $\beta = \{1.20, 1.28, 0.58\}$ for BFL, POP, and BB, respectively. For this problem, the maximum error occurs near the surface.

Although the interpolation boundary techniques support second-order-accurate flow past an isolated sphere, the computed velocities at grid points closest to the surface are not second-order-accurate. The surface error, L_2^S, was calculated and fitted to (8), and the resulting power-law exponents are $\beta = 0.56$ for BFL and $\beta = 0.64$ for POP. As noted in Section 1.3, a value of $\beta = 1$ is consistent with a second-order method for this measure. Although the estimates are arguably biased
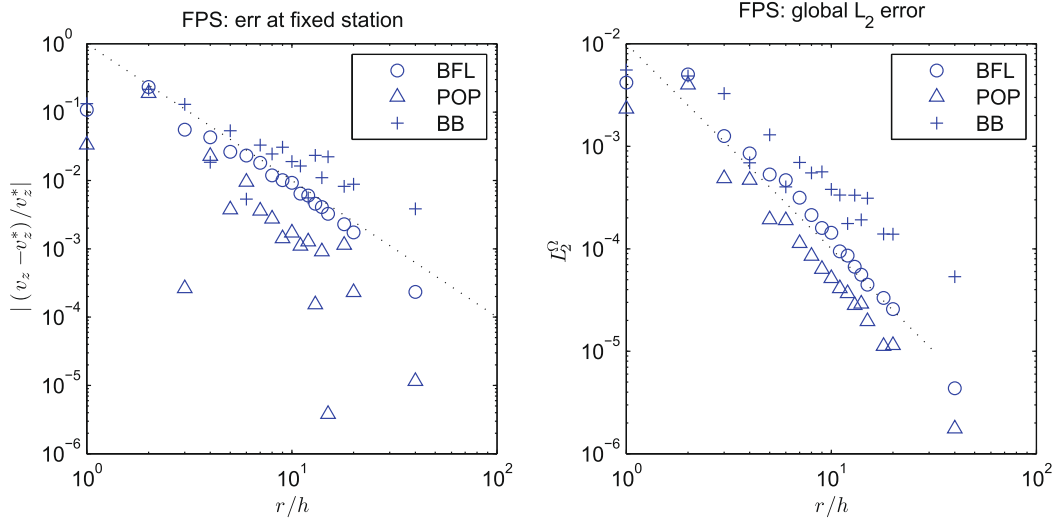
Fig. 5. Flow past an isolated sphere: (left) relative velocity error at a fixed station on the centerline (one half sphere radius from the stagnation point), and (right) global velocity L_2 error vs. grid resolution.
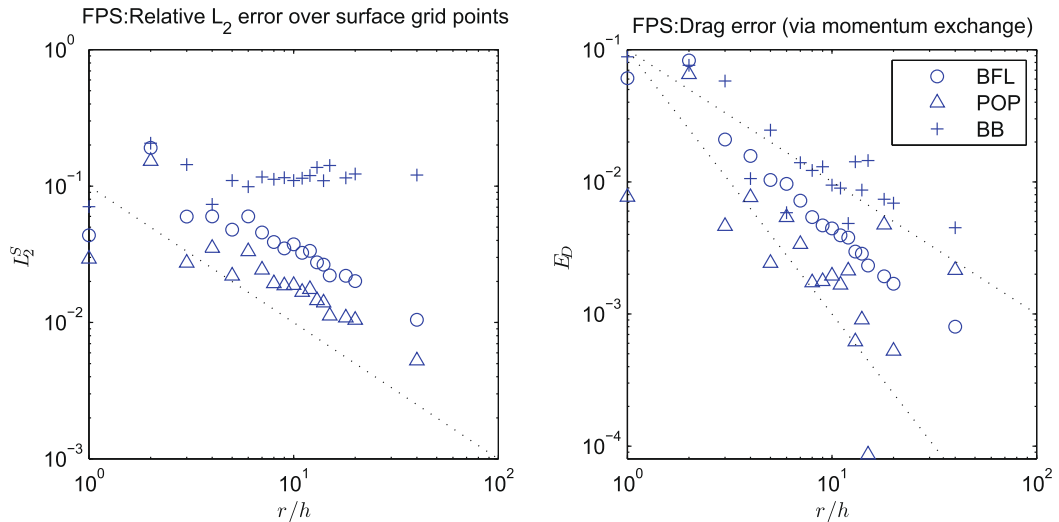

Fig. 6. Flow past an isolated sphere: (left) surface velocity L_2 error and (right) drag error vs. grid resolution.

downward by low-resolution data points, the trends shown in Fig. 6(a) appear consistent with something between first and second-order accuracy for L_2^S. The value for bounce back is $\beta = -0.05$, consistent with a first-order technique.

The accuracy at grid points near the surface does not degrade that of the general flow in this case, but it can affect calculations that rely upon surface velocities. An important case is that of the drag force. The total force acting on the sphere is well-known as a surface integral of the pressure and shear stress

$$F_D = \int_\Gamma (-pI + \rho v (\nabla u + \nabla u^T)) d\gamma$$

where Γ represents the surfaces of the boundaries in Ω. In the LB method, there is a concise procedure for approximating this force, known as the momentum-exchange technique, given by

$$F_D = \sum_{x_j \in S} \sum_{i \in V_j} e_i (f_i(x_j, t_{n+1}) + f_i^C(x_j, t)) \tag{12}$$

The f_i impinge on the surface and the f_i^C are reflected back on the opposite vector, so this expression describes the net momentum impinging on the surface per unit time. The technique was perhaps first presented by Ladd [37] and later by others, e.g. [38]. Ladd considered the case of a sphere discretized on a regular grid, which introduces a discretization error

of $O(h)$. He analyzed the drag error using the concept of an effective hydrodynamic radius, r_{eff}, where the Stokes drag formula is used to determine the ideal radius associated with the computed velocity and drag. If the sphere radius is given by $r_j = jh, j = 1, \ldots$, then the magnitude of the correction is given as $r_{eff} = r_j + 0.8h$ (see Hill et al. [39, p. 217]).

In the present work, the computed drag (12) is compared to Stokes' drag, $F_{St} = 6r\pi\mu U$, using the relative error $E_D = |(F_D - F_{St})/F_{St}|$. Fig. 6(b) shows the error for BFL is strictly decreasing and the errors for POP and bounce back are non-monotonically decreasing. E_D was fitted to Eq. (8) and the power-law exponents are $\beta = \{-1.34, -.99, -.84\}$ for BFL, POP, and bounce back, respectively. These values indicate the drag calculation is first-order-accurate for all three boundary techniques. Caiazzo and Junk [40] concluded that Eq. (12) is formally first-order-accurate, and suggested a modification to improve its accuracy, which involves averaging information among grid points adjacent to the surface. Most likely, it would be necessary to use information from at least a second layer of grid points away from the surface to achieve second-order accuracy in the drag calculation.

3. Quadratic flow past a sphere near a wall

Flow past a sphere near a wall exhibits several flow phenomena, including a recirculation cell around the sphere, and backflow between the sphere and wall. Our primary interest is the backflow region, which is representative of the pore spaces in more complex geometries. The recirculation cell is of less relevance because it is much larger than a typical pore.

Pasol et al. [42,41] have recently published exact solutions for a variety of such flows. We examine quadratic flow parallel to the wall, where the far-field flow is in the z direction with magnitude $v_z = x^2$. The wall is located at $x = 0$, the sphere is centered at $x = [\ell/r, 0, 0]$ and the sphere cap is at $x = [1 + \ell/r, 0, 0]$, where ℓ/r is the dimensionless distance between the sphere and wall. The case of $\ell/r = 1.18$ is described in detail in [41].

The ambient pressure distribution is characterized by a uniform gradient in the flow direction with zero-pressure at $z = 0$. Positive and negative pressure cells attach to the fore and aft surfaces of the sphere. These cells are defined by zero-pressure isosurfaces that extend away from the surface along the centerline, curve upward, and meet at a distance r above the sphere cap. The pressure cells contained between the zero-pressure isosurfaces and the sphere surface are opposite in sign to the general pressure field.

The velocity field is characterized by an elongated, toroidal recirculation cell wrapped around the sphere. A cross-section of the cell in the x–z plane shows two 2D vortices fore and aft of the sphere (Fig. 7). The central axis of recirculation lies below the sphere centerline, lifting the flow stagnation point above the centerline. Below the recirculation cell, the flow actually moves upstream between the sphere and wall.

We imposed the exact solution as Dirichlet conditions on a bounding box containing the sphere, to exclude the influence of far-field boundary errors. The LB boundary techniques were used to compute no-slip conditions on the wall and the sphere surface. The exact solution was also imposed as the initial condition everywhere. Note, the minimum distance between the sphere and wall, $\ell/r = 1.18$, is resolved with less than one grid space for $r/h < 6$. The convergence criterion (11) is the same as that for an isolated sphere.

The largest pressure errors occur on the sphere cap, in the region of maximum shear, and elsewhere near the surface. The error magnitude on the cap is largest for bounce back and least for POP. The largest velocity errors also occur over the sphere cap. Velocities near the wall and in the recirculation cell are relatively small and do not contribute much directly to global error measures. However, error measures are more volatile than in the case of flow past an isolated sphere and do not always converge as a simple power-law function. There is a threshold value of h required to resolved the recirculation cell, and this causes certain measures to converge in a nonlinear fashion. For example, the velocity magnitude at surface-adjacent grid points, given by the denominator of Eq. (10), is expected to converge as h^0. In fact it behaves as a step function in the interval $2 < r/h < 3$, converging as h^0 for $r/h > 3$. Therefore, we restrict the analysis of convergence to the range $r/h > 3$.

We confine our analysis of the error to the surface-adjacent grid points and to the backflow region between the sphere and wall, defined as $B = \{x_j | x \leqslant \ell, -r \leqslant y \leqslant r, -r \leqslant z \leqslant r\}$. In the backflow region, the recirculation cell pumps fluid between the sphere and wall opposite to the general flow direction. The L_2 velocity error in the backflow region is given by L_2^B, where the set of grid points, B, replaces Ω in Eq. (9). L_2^B converges more slowly than expected for a second-order method (Fig. 8(a)). The behavior is between first and second-order for POP and closer to first-order for BFL and BB. L_2^B is sensitive to details such as the location of streamlines relative to the surface because it is the sum of squared errors at each grid point. Alternative measures, such as the mean flux, are less sensitive to the location of streamlines and converge more quickly. The mean flux error is given by $\sum_B (v_z - v_z^*)/|B|$. Fig. 8(b) shows this error is more volatile than L_2^B, but arguably converges at a second-order rate for all three boundary techniques.

3.1. Velocity error at surface-adjacent grid points

The set of surface-adjacent grid points lies within $y_n < \sqrt{3}h$ of the sphere surface. Although the velocity at these points is proportional to y_n, the error at these points is essentially independent of y_n (Fig. 9). However, the error does depend on the boundary technique. For example, at a resolution of $r/h = 10$, the surface L_2 error is $L_2^S = \{0.021, 0.036, 0.123\}$ for POP, BFL, and BB, respectively, and these results are quite similar to the case of flow past an isolated sphere. However, for a given value
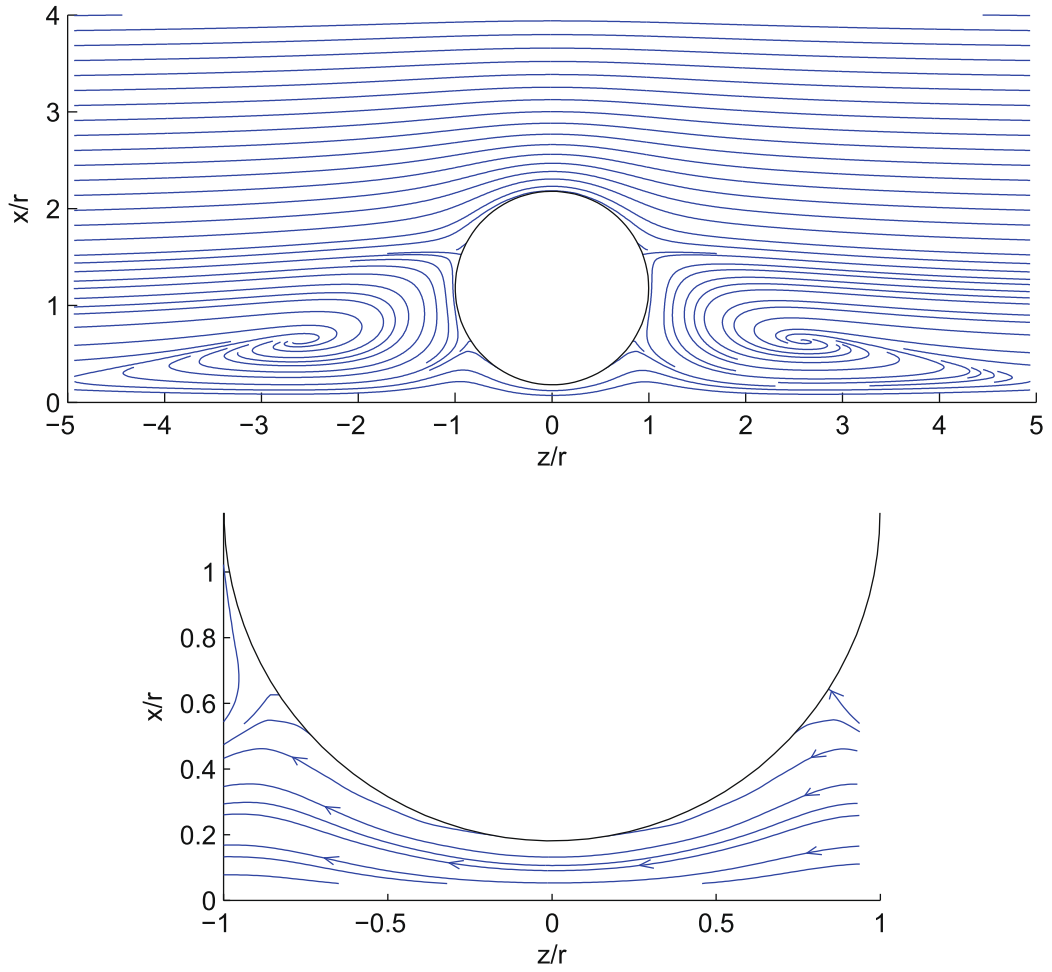
Fig. 7. Flow past a sphere near a wall: (top) cross-section of computational domain, and (bottom) close-up of the backflow region.
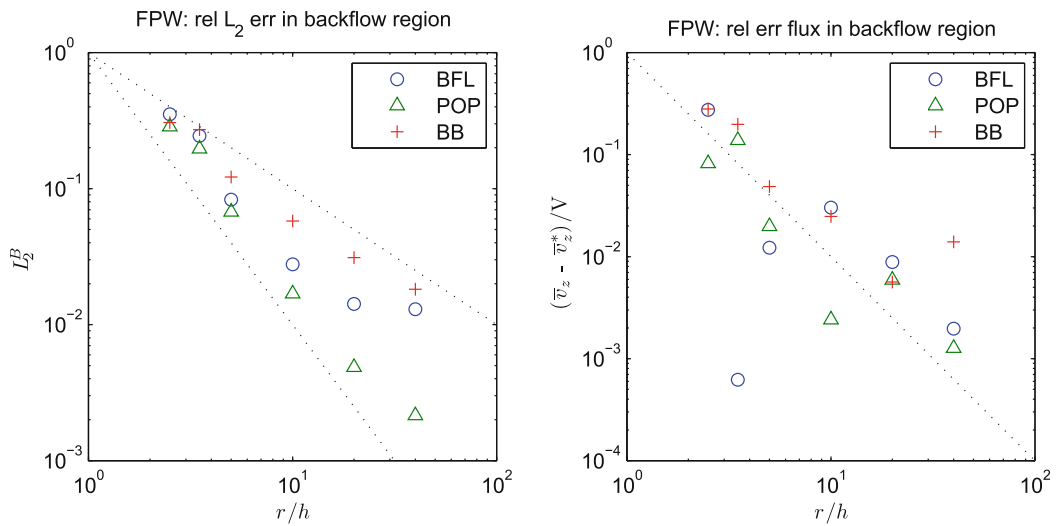

Fig. 8. Flow past a sphere near a wall: (left) velocity L_2 error and (right) mean flux error in backflow region. The mean flux error is relative to V, the mean flux computed from the exact solution at the highest spatial resolution.
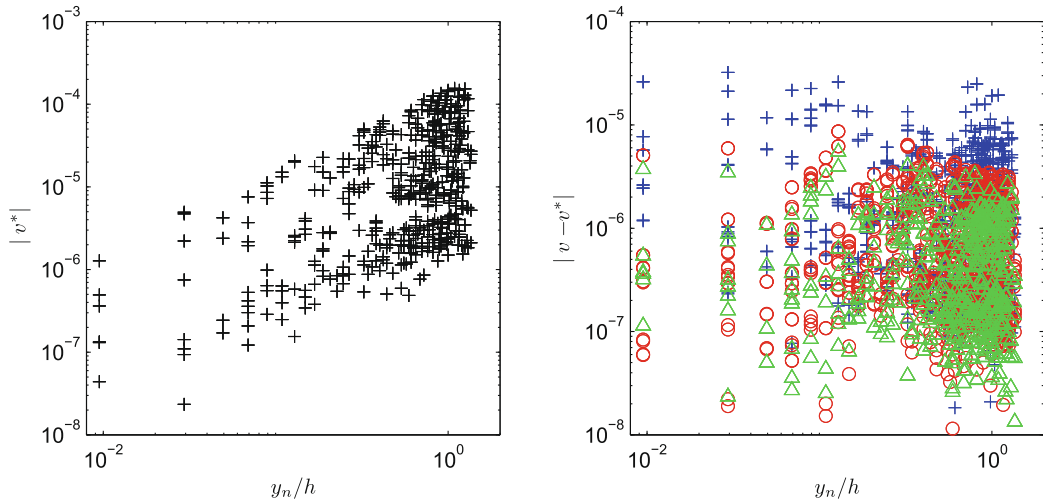
Fig. 9. Flow past a sphere near a wall: (left) velocity magnitude and (right) error at surface-adjacent grid points vs. distance to surface, for r/h = 10.
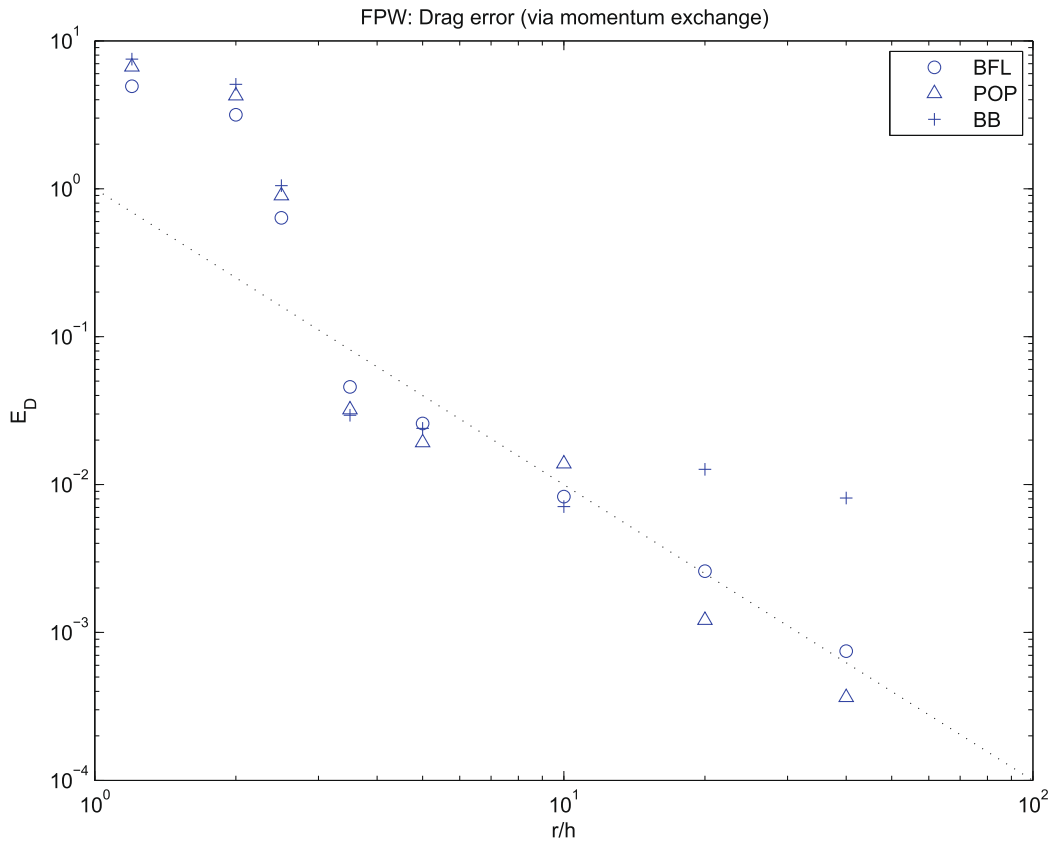

Fig. 10. Flow past a sphere near a wall: drag error vs. grid resolution.

of y_n, the variance in error magnitude is larger than for an isolated sphere, and the errors associated with the three techniques overlap to a much greater extent (compare Figs. 9 and 3).

The surface error, L_2^S, converges at a second-order rate using the interpolation techniques, POP and BFL, and at first-order using BB. The drag error, E_D, converges monotonically at second-order for POP, between first and second-order for BFL, and non-monotonically at first-order for bounce back (Fig. 10). Recall that L_2^S and E_D converged more slowly in the case of an isolated sphere, and that the drag calculation is theoretically only first-order accurate. Thus, the convergence behavior in this case deserves some comment.
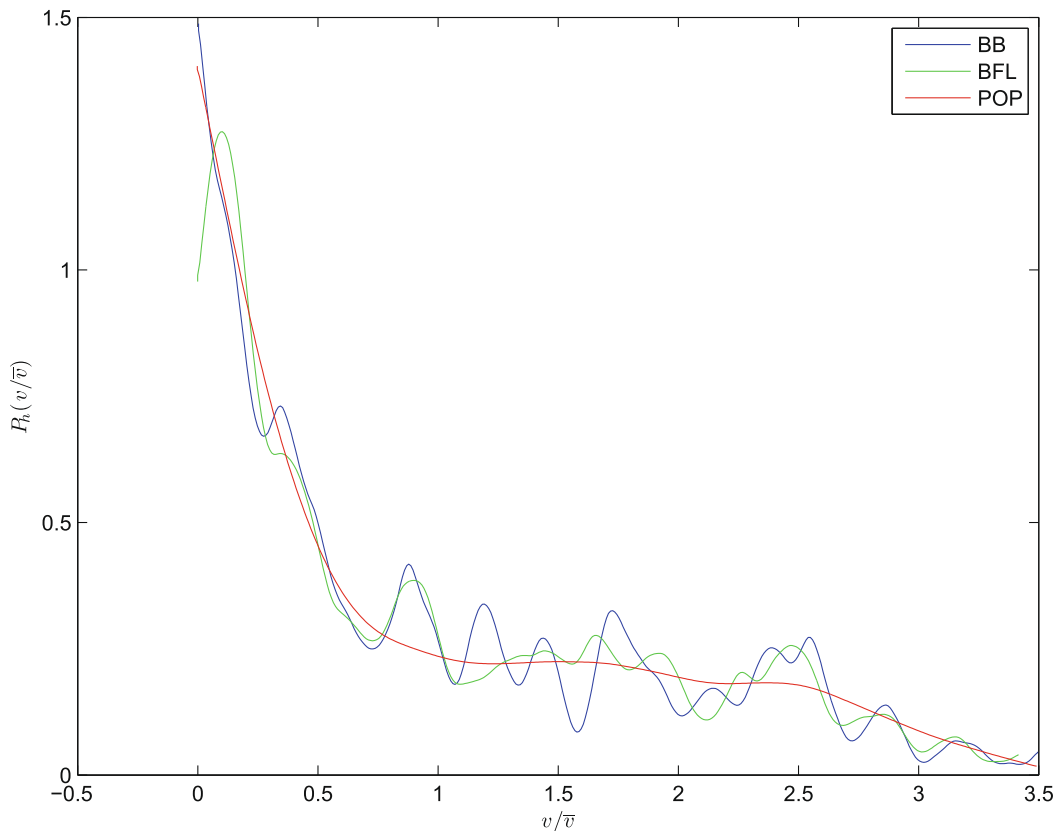
Fig. 11. BCC sphere array: filtered histograms of normalized *z* velocity component, *r/h* = 13.9.

The largest surface error occurs at the sphere cap and dominates the surface error measures. This is because the largest *z*-velocity occurs at the cap; the far-field velocity is quadratic in *x*, and the maximum value of *x* on the sphere is located at the cap. As the grid is refined, the surface-adjacent points at the cap have decreasing values of *x*, and so the velocity at these points decreases as h^2. At the remaining surface-adjacent points, the velocity and the error decrease more slowly. If L_2^S is computed over just the hemispherical surface opposite the sphere cap, the resulting error measure converges between first and second-order for POP and BFL.

4. Flow through a close-packed BCC array of spheres

Flow through periodic close-packed spheres exhibits recirculation and converging/diverging behavior, both prevalent in general porous media, even at small Reynolds numbers. Ring vortices form around sphere contact points but they are small compared to the sphere diameter and, unlike the earlier case of flow past a sphere near a wall, they make little contribution to the velocity distribution at small Reynolds numbers. Converging and diverging flows have a simple, symmetric structure occurring at pore junctions. Maier et al. [43] described converging flow in the pores of an FCC lattice as the junction of tube-like flow structures.

4.1. Smoothness of the velocity field

The velocity histogram, $P_h(v)$, is a discrete form of the velocity density function, giving the probability of finding a point in the fluid with a specified velocity, *v*. In the limit of high resolution, we expect $P_h(v)$ to be a piecewise-continuous smooth function. We expect a strong peak near *v* = 0 because the close-packed BCC array is dominated by near-surface flows. Secondary peaks are expected, based on earlier studies [43], but the general form of $P_h(v)$ approaches that of an exponentially decreasing function as the number of grid points is increased. In a periodic array, where the number of unique velocity values in the computational grid is limited by symmetry, $P_h(v)$ is characterized by high-frequency oscillations at grid resolutions typical of pore-scale simulations.

We found that the smoothness of $P_h(v)$ in practice depends on the boundary technique. To compare the effect of boundary techniques, we first applied a filter to reduce high-frequency noise. For the case of *r/h* = 13.9, the filtered histogram for

POP is quite smooth, with the quasi-exponential density typical of flow through sphere packings. However, the filtered histograms for BFL and bounce back still have spurious low-frequency oscillations that disappear when the grid is further refined. We infer that the spatial variation in velocity is smoother with the POP technique (Fig. 11).

4.1.1. Permeability of cubic arrays

Although there is no analytical solution for the fluid velocity in a periodic array, their permeability and drag have been well characterized analytically [44,45], and computationally [46,39,47] for dense arrays. The accuracy of the permeability calculation using LB methods has been studied by a number of researchers [43,39,31]. Maier et al. [43] reported grid convergence results on the permeability of an FCC array of spheres using the LB method with bounce back. As they decreased the grid spacing, their permeability estimate, $k(h)$, converged rapidly from above, dropped below the correct value, and then converged slowly from below. There are two competing effects on the error in permeability using bounce back. The first effect is simply the local error in approximating the flow at the boundary with Eq. (3). The second effect is a volume exclusion, or porosity, error caused by the $O(h)$ error in approximating the location of the boundary. Surprisingly, the direction of this error depends on whether the spheres are in contact. The ratio of stair-step to true volume of an isolated sphere is a non-monotonically decreasing function of r/h. Hence, the solid volume fraction of a dilute stair-step suspension is a decreasing function and porosity is an increasing function of r/h (i.e., the stair-step representation tends to underestimate the true porosity). In contrast, the porosity of a stair-step *close-packed* periodic array is a *decreasing* function of radius, because of the discretization of sphere contacts. This affects the porosity and permeability as $O(h^3)$ and, although this contribution drops off quickly, it has a significant effect at low-resolution. Maier et al. [43] found that as they refined the stair-step grid, the effective porosity of the close-packed FCC array dropped from $\phi = 29.7\%$ for $r/h = 5.5$ to $\phi = 26.1\%$ for $r/h = 22.5$. The Kozeny–Carman relation predicts a decrease of 50% in the permeability over this range of porosity while Maier et al. calculated a drop of 70%. (In the case of a BCC array, $\phi = 0.375$ for $r/h = 3.5$ and $\phi = 0.320$ for $r/h = 55.4$.)

Hill et al. [39] used the LB method with bounceback to compute flow through periodic arrays. They found that accuracy is a function not only of the grid resolution but the porosity of the array. They found $r/h = 1.88$ sufficient to calculate the average drag force in a moderately dilute array ($\epsilon = 0.80$), but used $r/h = 31.8$ in the FCC close-packing limit ($\epsilon = 0.36$) to achieve the desired accuracy. They noted that the close proximity of neighboring spheres requires streamlines to make much tighter turns, and makes the resulting gradients more difficult to resolve.

Pan et al. [31] calculated the permeability of BCC arrays using a multiple-time relaxation variant of the LB method and several boundary techniques, including bounce back and BFL. They presented grid convergence results indicating that if parameters of the LB method are correctly chosen, the interpolation techniques can support second-order-accurate flow calculations, but otherwise they support a lower rate of convergence.

4.2. Drag force calculated from global pressure gradient

For an array of uniform spheres, the average drag force per sphere can be calculated from the pressure gradient,

$$\overline{F}_D = [\epsilon/(1-\epsilon)](4/3)\pi r^3 \nabla p \tag{13}$$

and it is customary to normalize with Stokes' drag and the porosity,

$$F = \frac{\overline{F}_D}{\epsilon F_{St}} \tag{14}$$

where F_{St} is calculated using the superficial velocity, $\epsilon\bar{v}$, and $\bar{v}$ is the mean pore velocity from the LB simulation. As mentioned in [47], scaling F_D by $1/\epsilon$ actually gives the total force on the particle, friction drag plus buoyancy, but we use this expression for consistency with the earlier work [46]. The normalized average drag (14) involves a ratio of the pressure gradient to the velocity, which is inversely proportional to the permeability, as expressed in Darcy's law

$$\kappa\nabla p = -\mu\epsilon\bar{v} \tag{15}$$

Thus, both the normalized average drag and the permeability can be computed from the global flux and the pressure gradient, and both should therefore have the same order of accuracy as the LB method, if the boundary technique does not degrade the accuracy.

The average drag force in a close-packed BCC array (normalized unit cell dimension $2.31r$) was calculated for $Re = 0.01$, with grid resolutions in the range, $3.5 < r/h < 55.4$, and compared to the accurate value published by Zick and Homsy, $F^* = 162.9$, using the relative error, $E_D = (F - F^*)/F^*$. Fig. 12(a) shows the convergence of E_D depends on the boundary technique. Error magnitudes are similar at the lowest resolution, but differ by two orders of magnitude at the finest resolution, $r/h = 55.4$, for which $E_D = \{0.4\%, 0.03\%, 2\%\}$ for BFL, POP, and bounce back, respectively. The error for BFL behaves consistently as a second-order method, decreasing by approximately a factor of four as h is halved. The resulting trend appears linear on a log scale and only slightly less than second-order. The POP trend is somewhat less consistent but is also second-order. The bounce-back trend is nonlinear on a log scale and first-order. Ignoring the departures from linearity, a linear least-squares fit of E_D to the power-law function yields $\beta = \{-1.79, -1.05, -2.47\}$, for BFL, bounce back, and POP, respectively.

We also computed the grid convergence error for each boundary technique,

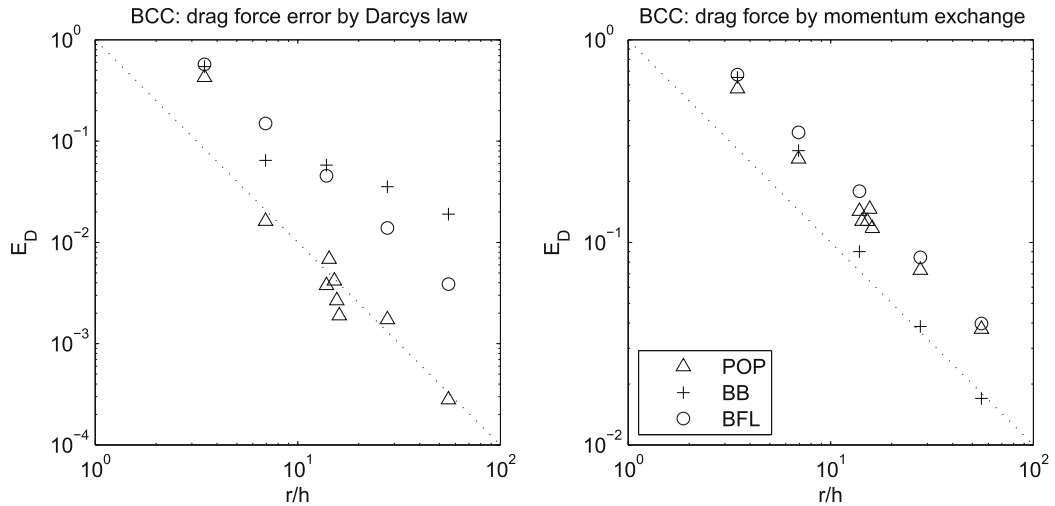$$\widehat{E_D} = |(F - \widehat{F})/\widehat{F}| \tag{16}$$

Fig. 12. BCC sphere array: drag error vs. grid resolution. (left) drag computed from global pressure gradient and mean velocity, (right) drag computed using momentum exchange.

Table 1
BCC sphere array: drag force relative error vs. grid resolution. The error E_D is relative to $F = 162.9$ [46]. $\widehat{E_D}$ and $\widehat{E_\kappa}$ are relative to values of $\widehat{F}$ and $\hat{\kappa}$ obtained with $r/h = 55.4$.

Technique	r/h	E_D Eq. (12)	E_D Eq. (14)	$\widehat{E_D}$ Eq. (14)	$\widehat{E_\kappa}$ Eq. (15)
BFL	3.46	0.6738	0.5738	0.5721	1.3370
BFL	6.93	0.3490	0.1495	0.1462	0.1712
BFL	13.86	0.1790	0.0454	0.0417	0.0435
BFL	27.71	0.0843	0.0139	0.0100	0.0101
BFL	55.43	0.0397	0.0039	0.0000	0.0000
BB	3.46	0.6517	0.5449	0.5534	1.2390
BB	6.93	0.2840	0.0645	0.0820	0.0893
BB	13.86	0.0901	0.0580	0.0382	0.0368
BB	27.71	0.0384	0.0356	0.0162	0.0159
BB	55.43	0.0170	0.0190	0.0000	0.0000
POP	3.46	0.5743	0.4267	0.4269	0.7448
POP	6.93	0.2586	0.0162	0.0165	0.0168
POP	13.86	0.1427	0.0038	0.0035	0.0035
POP	14.29	0.1272	0.0068	0.0066	0.0065
POP	15.16	0.1270	0.0042	0.0039	0.0039
POP	15.59	0.1461	0.0027	0.0029	0.0030
POP	16.02	0.1173	0.0019	0.0016	0.0016
POP	27.71	0.0730	0.0017	0.0015	0.0015
POP	55.43	0.0373	0.0003	0.0000	0.0000

where $\widehat{F}$ is the drag estimate obtained at the highest grid resolution for each technique. All boundary techniques have more favorable convergence behavior using $\widehat{E_D}$. The fitted power-law coefficients were $\beta = \{-1.93, -1.64, 2.78\}$ for BFL, bounce back, and POP, and may be compared with the coefficients in the preceding paragraph. Bounce back, in particular, is closer to second-order. This highlights the difficulty with using grid convergence behavior to infer the order of accuracy. The actual error, E_D, and the grid convergence error, $\widehat{E_D}$, are compared in Tables 1 and 2.

4.2.1. Drag force by momentum exchange

In certain applications (e.g., suspension flows), it is necessary to calculate the force imposed by the fluid on individual spheres from the local velocity field, and this is typically accomplished with the momentum-exchange technique (12) in the LB method. To understand the convergence of the resulting drag error, we calculated F using (12) and compared with F^* from Zick and Homsy [46]. The relative error at the lowest resolution was $E_D \approx 60\%$, and decreased to a value between 2% and 4% at the highest resolution (Fig. 12(b)). The convergence rate is approximately first-order for all three boundary techniques ($\beta = \{-1.02, -1.34, -0.97\}$, for BFL, bounce back, and POP). Thus, F has a lower order of accuracy when computed by (12) than when computed by (14). For the bounce-back method, the error trend is more linear on the log–log scale using (12).

Table 2
Random sphere packing: drag force and permeability relative error. $\widehat{E_D}$ and $\widehat{E_\kappa}$ are relative to values of $\widehat{F}$ and $\dot{\kappa}$ obtained with $r/h = 41.8$.

Technique	r/h	$\widehat{E_D}$ Eq. (12)	$\widehat{E_D}$ Eq. (14)	$\widehat{E_\kappa}$ Eq. (15)
BFL	2.62	0.6900	0.4655	0.8709
BFL	5.24	0.3936	0.2112	0.2677
BFL	10.47	0.1638	0.0653	0.0698
BFL	20.94	0.0495	0.0137	0.0139
BB	2.62	0.6263	0.3558	0.5523
BB	5.24	0.3227	0.1190	0.1351
BB	10.47	0.1170	0.0129	0.0131
BB	20.94	0.0288	0.0077	0.0076
POP	2.62	0.5954	0.2865	0.4015
POP	5.24	0.2893	0.0646	0.0690
POP	10.47	0.1148	0.0054	0.0055
POP	20.94	0.0367	0.0012	0.0012

5. Flow through a close-packed random array of spheres

Periodic arrays illustrate recirculation and converging/diverging flows under conditions of symmetry, and so it remains to characterize the effects of randomness and asymmetry. Much is known about the structure of random sphere packings. For example, Torquato [48] presented a set of structure functions describing the geometrical properties of monodisperse sphere packings. Many researchers have used simulation methods to generate random sphere packings in order to study their properties and to perform simulations of pore-scale flow (e.g., [43,49,50,39,51,52,47,31]).

Flow through random sphere packings is dominated by surface effects. The nearest-surface distribution function, a proxy for the pore-size distribution, is a half-Gaussian function with a peak close to zero. This distribution defines the convergence behavior of the flow simulations. At sufficiently low grid resolutions, a majority of the grid points are surface-adjacent grid points, which lie adjacent to the surfaces (assuming a regular grid). At higher resolution, the set of surface-adjacent points, S, is no longer a strict majority but remains a significant fraction of the total and supports the peak in the velocity distribution function near $v = 0$. In the range of grid resolutions relevant to pore-scale simulations, the accuracy of the simulation is tied to this set of grid points.

In the present work, fluid flow was simulated in an array of 125 uniform spheres packed randomly in a periodic cube of dimension $L = 4.78d$, to a porosity of 39%. A uniform pressure gradient was used to drive the flow to a Reynolds number of $Re = 0.05$. No-slip boundaries were applied on the sphere surfaces, and periodic conditions were applied at the box boundaries. (Sphere surfaces that protrude beyond the box boundary appear as periodic images intruding from the opposite boundary.) The flow was allowed to develop from initial conditions $v = 0$ everywhere until the convergence criterion (11) was satisfied. Flow was simulated for each boundary technique at five levels of spatial resolution, $r/h = \{2.6, 5.2, 10.5, 20.9, 41.8\}$.

5.1. Instability of POP technique

Flow through a random array of spheres is the only problem in which we found evidence of instability in the POP technique. The simulations were conducted at low-Reynolds numbers, ruling out the standard reason for developing instabilities. The onset of instability is gradual and manifests as a growing oscillation in velocity at lattice sites with especially complex boundary configurations. For example, lattice sites near sphere contacts may have a majority of their lattice vectors pointing into the spheres, often in an asymmetric pattern. At some of these sites, a growing oscillation in mass develops between two subsets of f_i over successive time steps. The instability does not appear to be correlated with severe mass imbalance.

An *ad hoc* procedure to suppress the instability was to apply bounceback at all grid points where more than $|V_j| > 9$ lattice vectors intersect the boundary. We concluded that the problem is not related to Mach number, nor is it strictly related to the number of lattice vectors intersecting the spheres at a particular lattice site, although this is a proximate cause. The POP technique showed no sign of instability on the earlier cases, including flow through a BCC array of spheres. This leads to the conclusion that asymmetry, in addition to complex boundaries, has some influence, although the precise mechanism remains unknown.

The failure of the POP technique highlights a more general problem in modeling flow through porous media. Many lattice sites have multiple boundaries where the LB method is expected to resolve flow in apertures of width h with entrance and exit velocities of different sign and magnitude. Obviously, one should not expect a real solution of the momentum equations from the LB method under such conditions.

5.2. Velocity distribution

Maier et al. presented results on the velocity density function in random close-packed spheres, using the LB method with bounce back. They showed that as the computational grid is refined, $P_h(v)$ converges to a quasi-exponential functional form with a peak near $v = 0$ and a maximum velocity on the order of $v_{max} \approx 10\bar{v}$ [43].
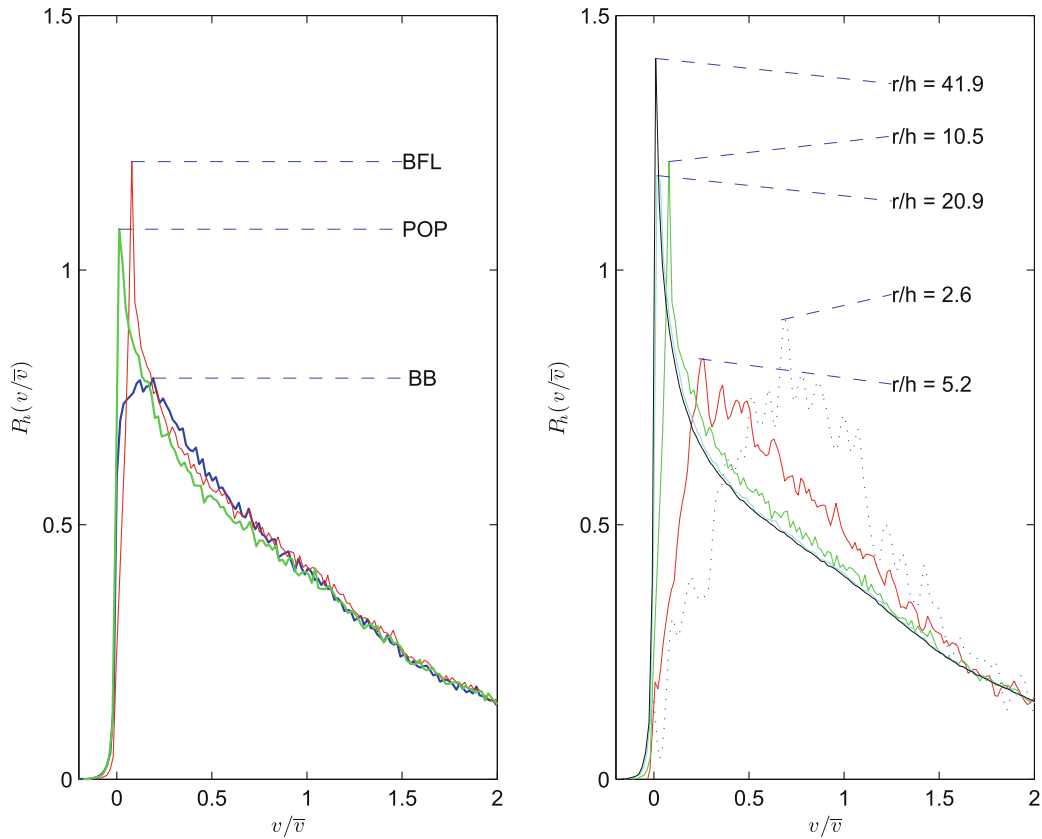
Fig. 13. Random sphere packing: histograms of normalized z velocity component (left) using different boundary techniques with $r/h = 10.5$, and (right) using different levels of spatial resolution with BFL technique.

The location of the peak in $P_h(v)$ is sensitive to the grid resolution. As h is decreased, the peak shifts toward $v = 0$ because surface-adjacent grid points support the peak and the velocity at these points approaches zero with h. The peak height also tends to increase as h is reduced to zero, for the same reason. Conversely, as h is increased, the surface-adjacent grid points are farther from the sphere surface, and this smears and shifts the peak to the right of $v = 0$. Fig. 13(b) illustrates the convergence of $P_h(v)$ using BFL.

The shape of P_h is already well approximated at a resolution of $r/h = 10.5$ (Fig. 13(a)). The peak height of P_h is converged at this resolution for BFL and POP. The interpolation techniques more accurately resolve velocity at surface-adjacent grid points, sharpening the peak and shifting it toward $v = 0$ relative to the results for bounce back, which are more smeared. In contrast, boundary techniques have a relatively minor effect on $P_h(v > \bar{v})$, which corresponds to the region of flow away from the surfaces. The maximum velocity converges to $v/\bar{v} \approx 7$ and the minimum to $v/\bar{v} \approx -0.2$ (Fig. 14).

Log plots of P_h (not shown) reveal that POP and bounceback have similar fractions of velocities near the extremes, and that BFL has slightly narrower range. The maximum velocity is lower than in [43] because of differences in the porosity and the size of the random packings.

5.2.1. Convergence of permeability estimate

There are a number of previous results on grid convergence of permeability in close-packed random arrays. The grid convergence error is given as

$$\widehat{E_\kappa} = (\kappa - \hat{\kappa})/\hat{\kappa} \tag{17}$$

where $\hat{\kappa}$ is the permeability value calculated at the highest available grid resolution.

Maier et al. [43] used the LB method with bounce back to calculate flow in a cylinder of diameter $7d$, packed randomly with uniform spheres to a porosity of 43%. They presented a grid-convergence result for the permeability at resolutions of $r/h = \{4.57, 9.14, 18.29, 36.57\}$, and found that for $r/h = 18.29$, the value of κ differed by 0.2% from that of $r/h = 36.57$.

Pan et al. [31] used a multiple-relaxation-time variant of the LB method to study the effect of various boundary techniques. They simulated flow in an array of 23 uniform spheres packed randomly in a periodic box to a porosity of 36% and presented grid convergence results for permeability. They found a relative error of 1% was attained at $r/h = 11.2$ for
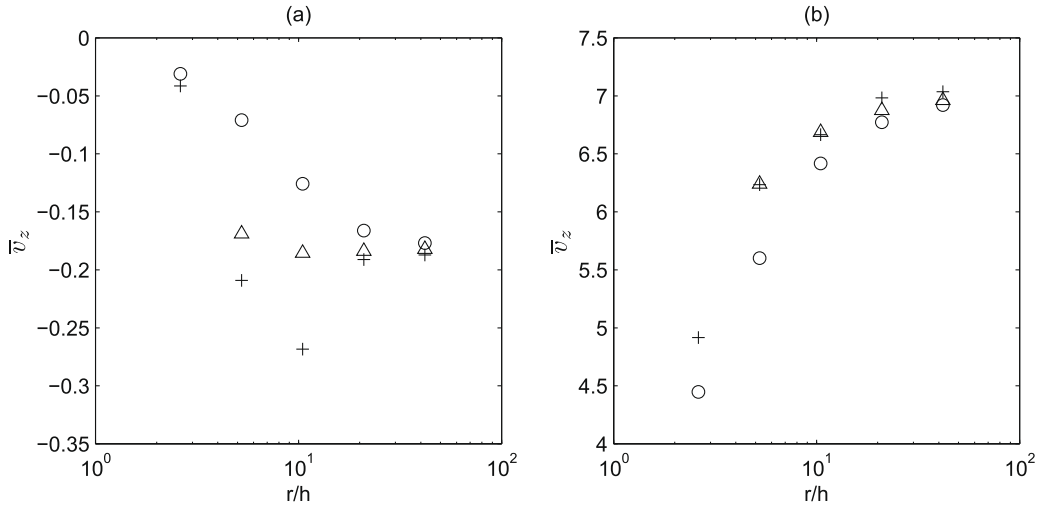
Fig. 14. Random sphere packing: (a) minimum and (b) maximum z velocity vs. grid resolution. ∘ = BFL, + = BB, △ = POP.
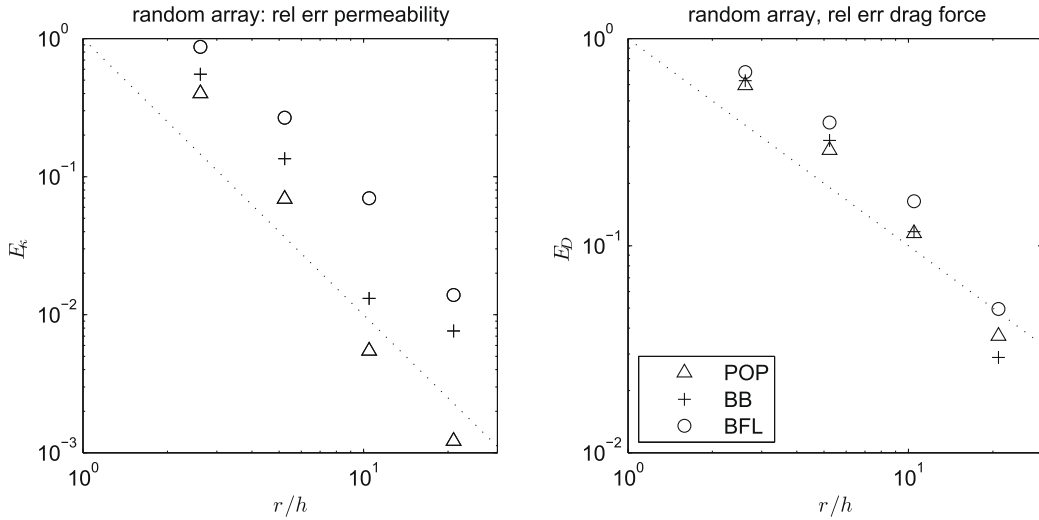

Fig. 15. Random sphere packing: (left) permeability error and (right) drag error vs. grid resolution.

BFL and bounce back, and this error was attained for all boundary techniques at $r/h = 16.8$. Their values of $\hat{\kappa}$ were obtained with $r/h = 35$.

In the present work, $\hat{\kappa}$ was computed for each boundary technique using $r/h = 41.8$. A relative error of 1% is attained for $r/h = 10.5$ using POP and bounce back, but this was not attained with BFL. The convergence trend is approximately second-order for all three boundary techniques (Fig. 15(a)). A linear least-squares fit of $\widehat{E_{\kappa}}$ to the power-law function yields exponents $\beta = \{-1.98, -2.19, -2.87\}$ for BFL, bounceback, and POP, respectively. The corresponding estimates for the BCC array (Section 4.2) are $\beta = \{-1.93, -1.64, -2.78\}$. Thus, grid convergence in the random and periodic arrays is about the same using interpolation techniques, and somewhat faster in the random pack using bounceback. For bounceback, randomness introduces additional error cancellation compared to the BCC array because the boundaries are aligned with the grid. The random array has many more pores and throats of varying size, and the flux errors in these structures tend to cancel one another.

The error associated with POP and bounceback seems to drop especially fast in the interval $5.2 \leqslant r/h \leqslant 10.5$. This is consistent with results in Section 5.2 showing that P_h is well approximated at a resolution of $r/h \approx 10$. This value of r/h may represent a threshold for permeability calculations because the majority of grid points are interior, while at a resolution of $r/h = 5.2$, the majority are surface-adjacent points. We can restate this idea in terms of the nearest-surface function as follows. The mean distance from a point in the fluid to the nearest-surface in our sphere packing is $\bar{s} \approx 0.066d$ (Fig. 16). If a sphere is resolved with only $r/h = 5$, we find that $\bar{s} < h$ and most grid points are surface-adjacent. Since the surface-adjacent points have lower accuracy than interior points, the permeability calculation should also be less accurate. At a resolution of $r/h = 10$, $\bar{s} > h$, and the average grid point is an interior point, so accuracy is closer to that of a strictly interior flow.
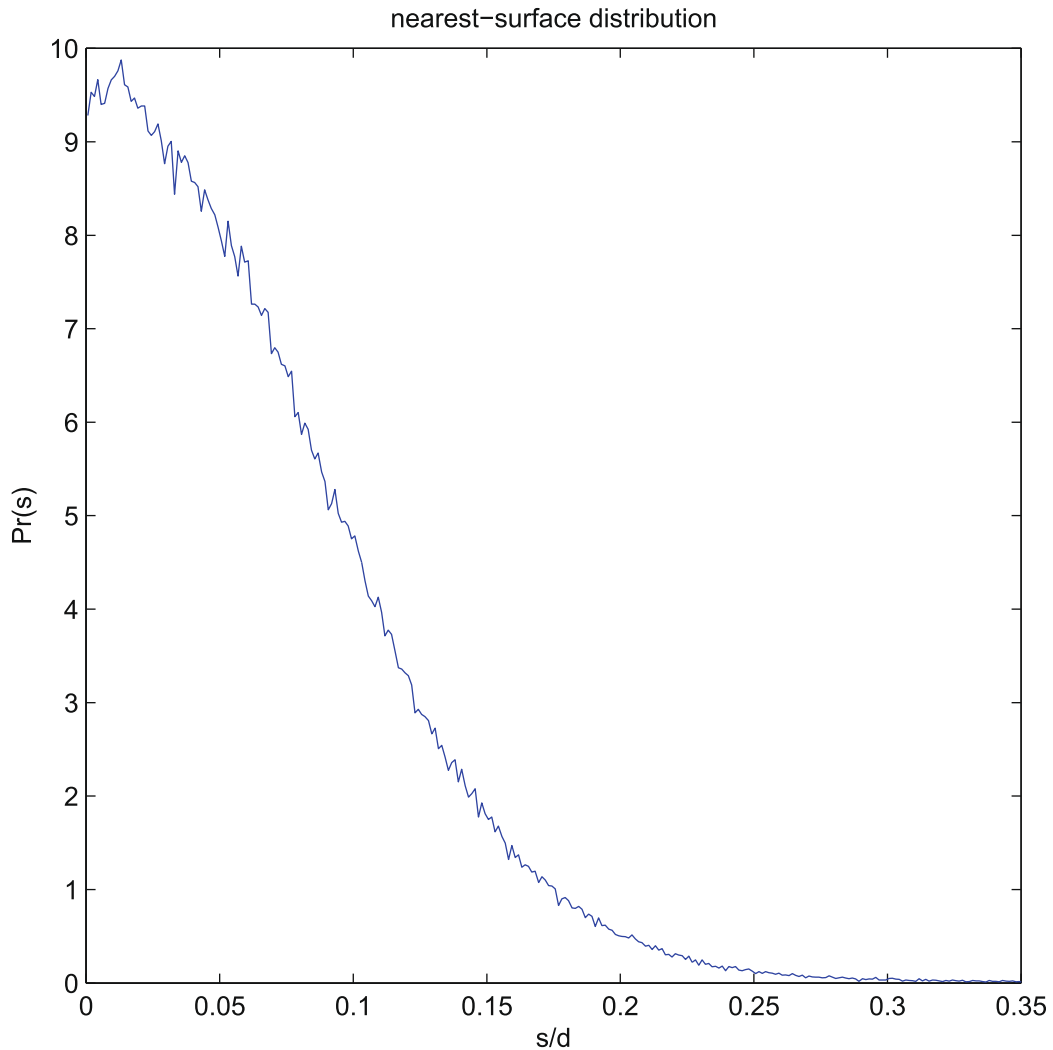
Fig. 16. Random sphere packing: nearest-surface distribution. Distance to nearest-surface is normalized by sphere diameter.

Table 3
Random sphere packing: normalized average drag force on a random array of uniform spheres. Values of $\widehat{F}$ obtained with $r/h = 41.8$.

Technique	$\widehat{F}$ Eq. (14)	$\widehat{F}$ Eq. (12)
BB	107.80	101.57
BFL	104.75	98.70
POP	105.30	99.05

5.2.2. Drag calculation

Grid convergence of the drag force was analyzed with the relative error (16), where $\widehat{F}$ was obtained using Eq. (12) and a grid resolution of $r/h = 41.8$ for each boundary technique. We found that $\widehat{E_D}$ converges at a rate less than second-order and greater than first-order in h for all three techniques (Fig. 15(b)). The estimates of the power-law exponent are $\beta = \{-1.27, -1.48, -1.34\}$ for BFL, bounceback, and POP, respectively. The corresponding results for the BCC array are $\beta = \{-1.02, -1.34, -0.97\}$. Thus the drag error converges somewhat faster in a random array. The explanation for this remains unknown, but error cancellation due to averaging of different grid-boundary orientations may play a role.

As mentioned in Section 4, the normalized drag for an array of uniform spheres can be calculated locally, using (12), or globally, using (14). These calculations are nominally first- and second-order-accurate, respectively. The estimates obtained with these two methods of calculation are compared in Table 3, using $r/h = 41.8$, and the difference is about 6%. Based on the results for a BCC array, for which we have an independent source of $\hat{\kappa}$ [46], the global method of calculation is probably more

accurate. The relative error associated with the global method of calculation is on the order of 1% at $r/h = 20$ (Fig. 15(a)) and the relative error associated with momentum-exchange is on the order of 3–5% at $r/h = 20$ (Fig. 15(b)). The drag estimates obtained with BFL and POP agree within 1% but differ from that of bounce back by approximately 2.5%. This is consistent with the observation in Pan et al., as well as the more general observation of Ladd, that the bounce back calculations converge toward something other than the true solution.

6. Hydrodynamic dispersion

Pore-scale flow simulations are important in the study of transport phenomena in porous media. Pore velocity fields can be used in a random walk simulation to recover transport behavior from Brownian particle displacements, or used directly in solving the convection–diffusion equation in the fluid subdomain of a porous medium. The sensitivity of such simulations to the flow solution and to the boundary techniques is therefore of interest.

In the present work we used random-walk simulations to model the motion of massless Brownian particles in the LB flow field described in Section 5. Particle motion was simulated by solving the stochastic Langevin equation independently for each particle in the ensemble. Particle position is not restricted to the LB grid points, but is determined independently for each particle by a forward Euler implementation of the stochastic Langevin equation,

$$x(t + \Delta t) = x(t) + v(x(t))\Delta t + \xi \sqrt{6 D_m \Delta t} \tag{18}$$

where ξ is a random vector on the surface of the unit sphere, and D_M is the coefficient of molecular self-diffusion. As the particles move through the pore space, they inherit their local velocity, $v(x(t))$, from the nearest LB grid point (via zero-order interpolation). Trajectories that bring particles to the solid boundary are truncated and the angle of departure is random. The solid boundary may be represented as a smooth surface or as a stair-step representation of the sphere surface. The sensitivity to this representation is discussed below. Particles exiting a periodic boundary re-enter the domain at the opposite boundary. The initial condition was a uniform distribution of particles in the pore spaces (one per grid cell).

We generated LB velocity solutions for the random walk simulations using $Re = 1$. The grid spacing of the velocity field determines the maximum particle time step. A CFL-like condition is imposed on Δt so that the maximum step length (con-
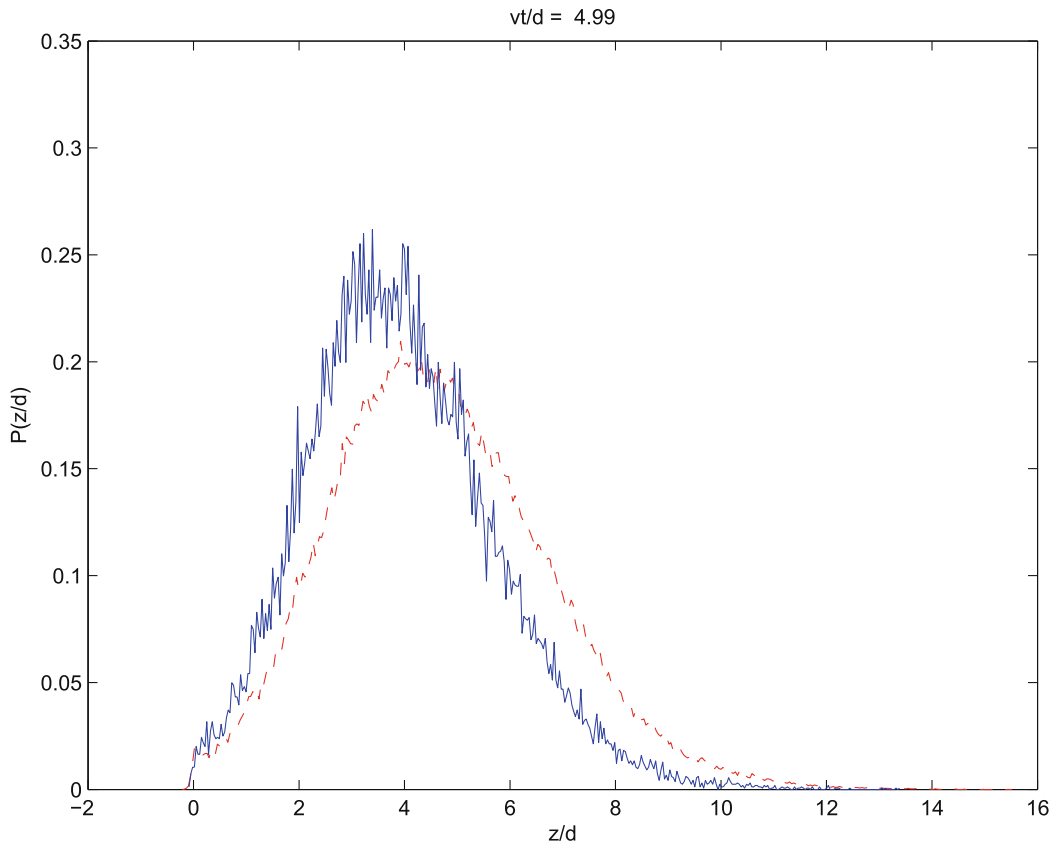

Fig. 17. Random sphere packing: z-displacement histogram of tracer particles (propagator function) at $t = 5d/\bar{v}$ using $Re = 1$ and $Pe = 476$. Solid line: $r/h = 5.2$, dashed line: $r/h = 10.5$. Displacement distance is normalized by sphere diameter.

vective + random) is less than $h/2$. In the case of r/h = 10.5, a particle with local velocity $\bar{v}$ has a convective displacement of $v(x(t)) \approx 0.25h$, which is similar in magnitude to its random displacement, $\xi\sqrt{6D_m\Delta t}$.

For the purposes of dispersion calculations, the computational domain is treated as a *periodic* random packing, where tracer particles are allowed to explore periodic images and potentially recorrelate with their initial velocity. The dispersion coefficients under these conditions do not represent a simple random array of spheres, and are in fact larger than would be obtained in a simple random array of the same packing density. For a more complete discussion of the effect of periodic boundaries on the dispersion coefficient, see [53]. The duration of each simulation was $t = 10d/\bar{v}$, which is the time for a particle traveling at the mean pore velocity to move a distance of 10 sphere diameters. Since the length of the sphere packing was $4.78d$, many tracer particles had sufficient time to traverse its full length, and a few of these rediscover their original velocity. Thus, after $t > 2d/\bar{v}$, the dispersion coefficients begin to reflect the effect of periodicity. This effect is unrelated to the fluid boundary techniques or the treatment of the sphere surfaces in the random walk.

6.1. Propagator function

The density function of tracer particle displacements is known as the propagator function, given here as $P(z)$, where z denotes the displacement in the flow direction. At very small values of time ($t \ll d/\bar{v}$), the shape of $P(z)$ is closely approximated by the velocity density function, $P_h(v)$. With increasing t, the particle ensemble gradually decorrelates with the initial velocity distribution, and $P(z)$ approaches a Gaussian distribution.
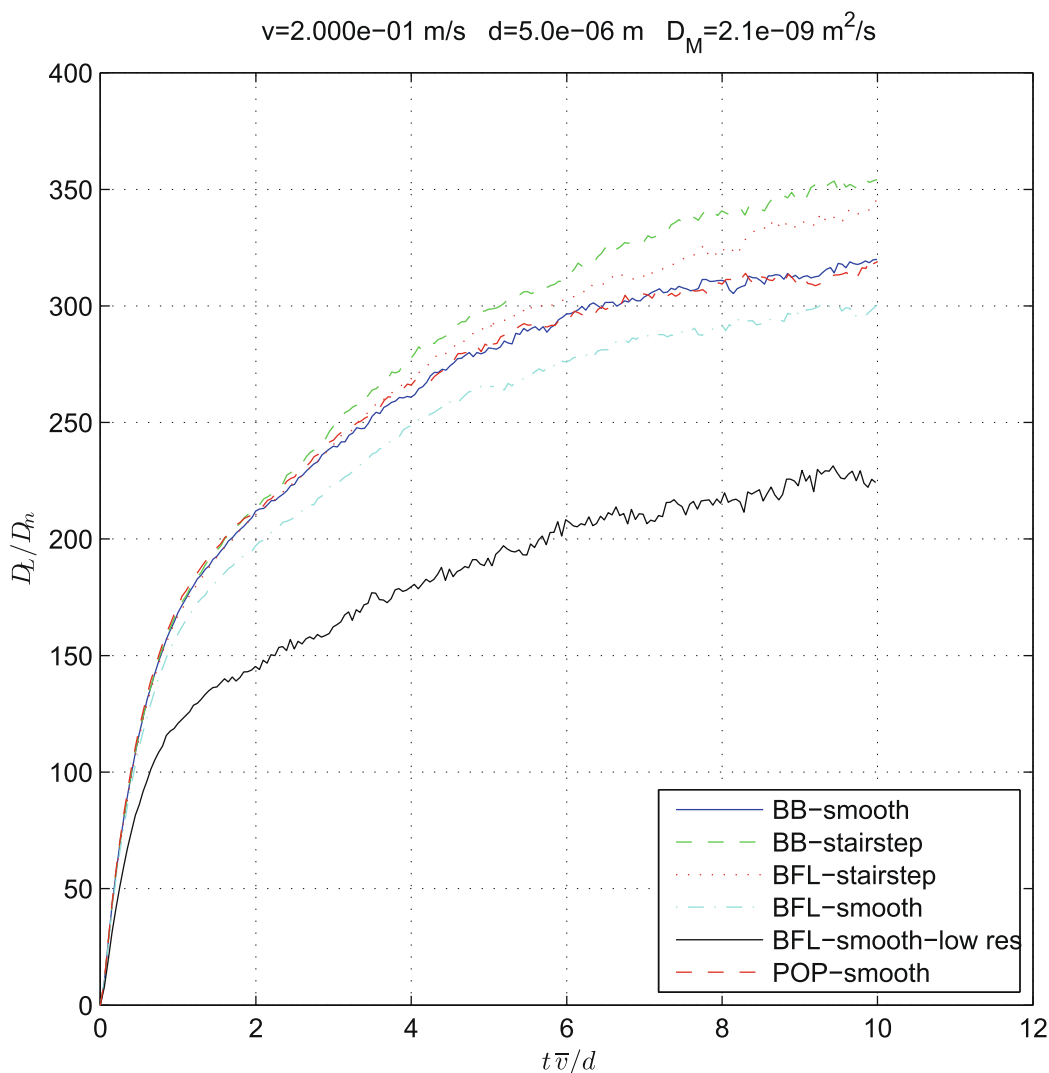

Fig. 18. Random sphere packing: longitudinal dispersion coefficient vs. time using different representations of the sphere surface. BB, BFL, and POP denote the boundary technique used in the fluid flow simulation. Smooth and stairstep denote the surface representation used in the random-walk simulation. All simulations used Re = 1, Pe = 476 and resolution of r/h = 10.5 except that denoted as low-resolution, which used r/h = 5.2.

Table 4
Random sphere packing: dispersion coefficients obtained with different velocity boundary techniques and surface representations. Values of D_L and D_T obtained at $t = 10d/\bar{v}$.

Surface representation		r/h	Dispersion coefficient	
LB flow	Random walk		D_L/D_M	D_T/D_M
Stairstep (BB)	Smooth	10.5	320	20.3
Stairstep (BB)	Stairstep	10.5	354	20.1
Smooth (BFL)	Stairstep	10.5	346	19.2
Smooth (BFL)	Smooth	10.5	300	17.8
Smooth (BFL)	Smooth	5.2	224	13.5
Smooth (POP)	Smooth	10.5	319	20.6

We are interested in the sensitivity of $P(z)$ to the accuracy of the fluid velocities and, in particular, to the boundary technique used in the flow simulation. We therefore performed random-walk simulations using velocity fields obtained with the different boundary techniques, and compared the resulting $P(z)$. We made these comparisons at several values of the dimensionless time $t\bar{v}/d = \{0.5, 1, 5, 10\}$ based on velocity fields obtained with resolution r/h = 10.5. However, we found no qualitative difference among the $P(z)$ based on boundary technique or the value of t. We did find that at $t = 10\, d/v$, the peak of $P(z)$ is slightly smeared by bounce back, compared to BFL, resulting in a 2–3% difference in peak height.

We did find a major difference in the propagator based on grid resolution. The propagator obtained with $r/h = 5$ is noticeably less dispersed (Fig. 17) and this translates to a lower dispersion coefficient, quantified in the next section.

6.2. Dispersion coefficient

Previous work using random-walk simulation suggests the calculated dispersion coefficient is sensitive to the grid resolution. Maier et al. [53] found the longitudinal dispersion coefficient increased with r/h over the range $5.5 \leqslant r/h \leqslant 29.5$ in a random packing of 100 spheres ($\epsilon = 0.36, \ Pe = 1142$). They concluded that grid independence was achieved at $r/h \approx 15$. The results were obtaining using bounce back and a stair-step representation of the boundary in the random walk.

Time-dependent dispersion coefficients were computed from particle displacements up to a dimensionless time of $td/\bar{v} = 10$ according to the formula

$$D_L(t) = D_{zz}(t) = \frac{1}{2N} \frac{d}{dt} \sum_{i=1}^{N} \left(\Delta z_i - \overline{\Delta z_i}\right)^2 \tag{19}$$

where $\Delta z = z(t) - z(0)$ corresponds to displacements in the flow direction and D_L is the longitudinal dispersion coefficient. $D_T(t)$ denotes the dispersion coefficient in the x direction, transverse to the flow. The time-dependent coefficients are plotted in Fig. 18 and their terminal values are tabulated in Table 4.

The dispersion coefficient increases with grid resolution of the velocity field. At a resolution of $r/h = 5.2$, the terminal value was $D_L/D_M = 224$, whereas at a resolution of r/h = 10.5, the value was $D_L/D_M = 300$ (results are based on the velocity fields obtained with the BFL boundary technique).

The terminal coefficients obtained with POP and bounce back are both $D_L/D_M \approx 320$. This value is about 4% higher than with BFL. A possible explanation is that the velocity fields from POP and bounceback have a higher maximum, and the width of the velocity distribution is correlated with the magnitude of dispersion [54]. The 4% difference due to boundary technique can be compared to the effect of random packing variation. The coefficient of variation (CV) in D_L due to random packing variation was found to be 2% in [54], where CV is the ratio of the standard deviation in D_L to the mean taken over a sample of random packed beds.

We are also interested in the sensitivity of D_L to the use of curved boundaries versus stair-step boundaries in the Langevin method. It has been suggested that pore-scale simulations of dispersion tend to underestimate experimental results because the surface area associated with a stair-step representation of the sphere surface reduces the hydraulic radius of the simulated pores, and that the resulting dispersion coefficients should therefore correspond to a smaller Peclet number (and Reynolds number) [55]. If this were the case, one would expect a smooth representation of the sphere surface to yield a larger dispersion coefficient. In fact, it yields a smaller one. The coefficients obtained with a stair-step representation in the random-walk simulation are about 10% larger than those obtained with a smooth representation. This result is obtained regardless of whether the underlying velocity field was also obtained on stair-step grid or using a boundary interpolation technique. In the present case, the value of $D_L/D_M = 355$ was obtained using a stair-step representation in the random walk and in the velocity simulation, compared with $D_L/D_M = 322$ obtained with a smooth representation in the random-walk and velocity simulations. Therefore, the stair-step representation does not appear to account for the difference between simulation and experiment. However, it is possible that other numerical artifacts connected with the random-walk method might play a role. Alternatively, it is possible that the simulation results correctly reflect differences in the dispersion coefficient between small, well-packed non-retentive sphere packings, typical of simulations, and larger experimental packings characterized by some degree of preferential flow and solute retention.

7. Conclusions

Pore-scale flows are dominated by surface effects. At low grid resolution, surface nodes may even outnumber interior nodes. The accuracy at surface nodes is often less than second-order, regardless of the boundary technique. However, the order of accuracy at these nodes does not necessarily degrade accuracy in the bulk flow away from the surface. Where the flow is well-resolved and gradients are not too large, interpolation boundary techniques support second-order-accurate interior flows. Where these conditions are not satisfied, they degrade accuracy to something less than second-order.

Measures such as the drag force and hydraulic permeability may have different convergence behavior than the global L_2 error, depending on a number of factors. Drag or permeability calculations based on the global pressure gradient and mean velocity depend more on the accuracy of interior flows than on the accuracy of velocities near the surfaces. These calculations are also affected by error cancellation, unlike the global L_2 error. If the drag is calculated by momentum-exchange, using surface-adjacent grid points, the result depends on the accuracy of near-surface flows, where the convergence is typically closer to first-order. However, we have identified one case in which the nominally first-order-accurate momentum-exchange technique achieves second-order behavior, flow past a sphere near a wall, and another case where it achieves better than first-order behavior, flow through a BCC array of spheres.

A particular error measure may not behave as a simple power-law function of grid spacing if important flow features are unresolved at low resolution. In the case of flow past a sphere near a wall, the recirculation cell is an important feature and a number of grid cells are required to represent rotational flow. Even a crude resolution of the cell noticeably improves convergence of the error measures. In a close-packed array of spheres, the average pore aperture is a small fraction of the sphere diameter, and not even the major flow paths are well-resolved at low resolution. Grid convergence of the permeability is achieved when the average aperture dimension, $\bar{s}$, is resolved with more than a single grid cell. (The resolution required to achieve grid convergence of the permeability to within 1% is $r/h \approx 10$).

The main question addressed in this work is whether interpolation boundary techniques can reduce grid resolution requirements in a pore-scale simulation. The evidence from past and present results seems generally affirmative, depending on the particular problem, the choice of boundary technique (and various LB parameters), and the range of resolution available. The case of flow past a sphere near a wall demonstrates that there is a threshold for resolution of certain flow structures, below which little is gained from an interpolation technique, and above which the advantage increases with grid resolution. This example represents a case where a first-order-accurate method for computing the local drag achieves second-order behavior.

The accuracy of an interpolation technique must be weighed against its relative complexity. The calculation of f_i is especially simple with the bounce back technique, but more importantly, the physical domain is easily represented for the purposes of calculation by coloring the grid cells to represent solid boundaries. The drawback is that one commits an $O(h)$ error in such representations. (This may render the accuracy of the boundary technique moot.) On the other hand, calculating the f_i is somewhat more complicated with BFL, POP, or another interpolation technique and there is still greater complexity associated with computing the ratios q_{ji} for an arbitrary geometry. We disagree with the assertion in [30] that boundary techniques which solve equations for the distribution function at fluid nodes adjacent to the solid surfaces "were found [by the community at large] to be overly complicated in the general case ..." and rather suggest that it is the greater complexity associated with the task of locating the boundary relative to the grid, especially in a dynamic context, that acts as a deterrent. To be clear, the deterrent is not the computational complexity (which is merely $O(n)$, where n is the number of grid nodes) but rather that of the logic required to process the q_{ij} and the data structures to store them. This complexity makes the use of interpolation boundary techniques less attractive to first-time code developers.

The argument for interpolation techniques becomes increasingly strong as the grid resolution and turnaround time are increased, and where near-surface and secondary flows are of particular importance. Near the threshold required for resolving secondary flows, however, interpolation techniques will have only a minor effect on the local solution.

References

[1] D. Zhang, R. Zhang, S. Chen, W.E. Soll, Pore scale study of flow in porous media: scale dependency, REV, and statistical REV, Geophysical Research Letters 27 (8) (2000) 1195.
[2] R.D. Hazlett, Simulation of capillary-dominated displacements in microtomographic images of reservoir rocks, Transport in Porous Media 20 (1995) 21–35.
[3] R.S. Maier, R.S. Bernard, Accuracy of the lattice-Boltzmann method, International Journal of Modern Physics C 8 (4) (1997) 747–752.
[4] D. Kandhai, A. Koponen, A. Hoekstra, M. Kataja, J. Timonen, P.M.A. Sloot, Implementation aspects of 3D lattice-BGK: boundaries, accuracy, and a new fast relaxation method, Journal of Computational Physics 150 (1999) 482.
[5] M. Wang, J. Wang, N. Pan, S. Chen, J. He, Three-dimensional effect on the effective thermal conductivity of porous media, Journal of Physics D: Applied Physics 40 (2007) 260–265.
[6] M. Yoshino, T. Inamuro, Lattice-Boltzmann simulations for flow and heat/mass transfer problems in a three-dimensional porous structure, International Journal for Numerical Methods in Fluids 43 (2) (2003) 183–198.
[7] B. Rotenberg, I. Pagonabarraga, D. Frenkel, Dispersion of charged tracers in charged porous media, Europhysics Letters 83 (3) (2008) 34004.
[8] Hlushkou et al, Pore-scale dispersion in electrokinetic flow through a random sphere packing, Analytical Chemistry 79 (1) (2007) 113–121.
[9] M. Wang, S. Chen, Electroosmosis in homogeneously charged micro- and nanoscale random porous media, Journal of Colloid and Interface Science 314 (1) (2007) 264–273.
[10] M. Reider, J. Sterling, Accuracy of discrete-velocity BGK models for the simulation of the incompressible Navier–Stokes equation, Computers and Fluids 118 (4) (1995) 459.
[11] J.D. Sterling, S. Chen, Stability analysis of lattice-Boltzmann methods, Journal of Computational Physics 123 (1996) 196.

[12] H. Chen, S. Chen, W.H. Matthaeus, Recovery of the Navier–Stokes equations using a lattice-gas Boltzmann method, Physical Review A 45 (8) (1992) R5339–R5342.
[13] R. Cornubert, D. d'Humières, D. Levermore, A Knudsen layer theory for lattice gases, Physica D 47 (1991) 241–259.
[14] D.P. Ziegler, Boundary conditions for lattice-Boltzmann simulations, Journal of Statistical Physics 71 (5–6) (1993) 1171–1177.
[15] I. Ginzbourg, P.M. Adler, Boundary flow condition analysis for the three-dimensional lattice-Boltzmann model, Journal of Physics II France 4 (1994) 191–214.
[16] D.R. Noble, S. Chen, J.G. Georgiadis, R.O. Buckius, A consistent hydrodynamic boundary condition for the lattice-Boltzmann method, Physics of Fluids 7 (1) (1995) 203–209.
[17] P.A. Skordos, Initial and boundary conditions for the lattice-Boltzmann method, Physical Review E 48 (6) (1993) 4823–4842.
[18] R.S. Maier, R.S. Bernard, D.W. Grunau, Boundary conditions for the lattice-Boltzmann method, Physics of Fluids 8 (7) (1996) 1788.
[19] S. Chen, D. Martinez, R. Mei, On boundary conditions in lattice-Boltzmann methods, Physics of Fluids 8 (9) (1996) 2527–2536.
[20] Q. Zou, X. He, On pressure and velocity boundary conditions for the lattice-Boltzmann BGK model, Physics of Fluids 9 (6) (1997) 1591–1598.
[21] O. Filippova, D. Hanel, Grid refinement for lattice-BGK models, Journal of Computational Physics 147 (1) (1998) 219–228.
[22] R. Mei, W. Shyy, D. Yu, L.-S. Luo, Lattice-Boltzmann method for 3D flows with curved boundary, Journal of Computational Physics 161 (2) (2000) 680–699.
[23] X. He, L.-S. Luo, M. Dembo, Some progress in lattice-Boltzmann method. Part 1. Nonuniform mesh grids, Journal of Computational Physics 129 (1996) 357.
[24] X. He, G. Doolen, Lattice-Boltzmann method on curvilinear coordinates system: flow around a circular cylinder, Journal of Computational Physics 134 (2) (1997) 306–315.
[25] R. Mei, W. Shyy, On the finite difference-based lattice-Boltzmann method in curvilinear coordinates, Journal of Computational Physics 143 (2) (1998) 426–448.
[26] M. Rohde, J.J. Derksen, H.E.A. Van den Akker, Volumetric method for calculating the flow around moving objects in lattice-Boltzmann schemes, Physical Review E 65 (5) (2002) 056701/1-1.
[27] R. Verberg, A.J.C. Ladd, Accuracy and stability of a lattice-Boltzmann model with subgrid scale boundary conditions, Physical Review E 65 (1) (2002) 016701/1–016701/16.
[28] M. Junk, Z. Yang, Asymptotic analysis of lattice-Boltzmann boundary conditions, Journal of Statistical Physics 121 (112) (2005) 3–35.
[29] M. Rohde, D. Kandhai, J.J. Derksen, H.E.A. Van den Akker, Improved bounce-back methods for no-slip walls in lattice-Boltzmann schemes: theory and simulations, Physical Review E 67 (6) (2003) 66703-1–66703-10.
[30] B. Chun, A.J.C. Ladd, Interpolated boundary condition for lattice-Boltzmann simulations of flows in narrow gaps, Physical Review B75 (2007) 066705.
[31] C. Pan, L.-S. Luo, C.T. Miller, An evaluation of lattice-Boltzmann schemes for porous medium flow simulation, Computers and Fluids 35 (8–9) (2006) 898–909.
[32] I. Ginzburg, D. d'Humieres, Multireflection boundary conditions for lattice-Boltzmann models, Physical Review E 68 (6) (2003) 66614-1–66614-30.
[33] R.B. Bond, C.C. Ober, P.M. Knupp, S. Bova, Manufactured solution for computational fluid dynamics boundary condition verification, AIAA Journal 45 (9) (2007) 2224–2236.
[34] C.J. Roy, Grid convergence error analysis for mixed-order numerical schemes, AIAA Journal 41 (2003) 595–604.
[35] B. Gustafsson, The convergence rate for difference approximations to mixed initial boundary value problems, Mathematics of Computation 29 (1975) 396–406.
[36] M. Bouzidi, M. Firdaouss, P. Lallemand, Momentum transfer of a Boltzmann-lattice fluid with boundaries, Physics of Fluids 13 (11) (2001) 3452–3459.
[37] A.J.C. Ladd, Numerical simulations of particulate suspensions via a discretized Boltzmann equation, Journal of Fluid Mechanics 271 (1994) 285–339.
[38] R. Mei, D. Yu, W. Shyy, L.-S. Luo, Force evaluation in the lattice-Boltzmann method involving curved geometry, Physical Review E 65 (4) (2002) 041203/1–041203/14.
[39] R.J. Hill, D.L. Koch, A.J.C. Ladd, The first effects of fluid inertia on flows in ordered and random arrays of spheres, Journal of Fluid Mechanics 448 (2001) 213–241.
[40] A. Caiazzo, M. Junk, Boundary forces in lattice-Boltzmann: analysis of momentum exchange algorithm, Computers and Mathematics with Applications 55 (7) (2008) 1415–1423.
[41] L. Pasol, A. Sellier, F. Feuillebois, A sphere in a second degree polynomial creeping flow parallel to a wall, Quarterly Journal of Mechanics and Applied Mathematics 59 (4) (2006) 587–614.
[42] L. Pasol, M. Chaoui, S. Yahiaoui, F. Feuillebois, Analytical solutions for a spherical particle near a wall in axisymmetrical polynomial creeping flows, Physics of Fluids 17 (7) (2005) 073602.
[43] R. Maier, D.M. Kroll, H.T. Davis, R. Bernard, Simulation of flow in bead packs using the lattice-Boltzmann method, Physics of Fluids 10 (1) (1998) 60.
[44] H. Hasimoto, On periodic fundamental solutions of Stokes equations and their application to viscous flow past cubic array of spheres, Journal of Fluid Mechanics 5 (Part 2) (1959) 317–328.
[45] A.S. Sangani, A. Acrivos, Slow flow through a periodic array of spheres, International Journal of Multiphase Flow 8 (4) (1982) 343–346.
[46] A.A. Zick, G.M. Homsy, Stokes flow through periodic arrays of spheres, Journal of Fluid Mechanics 115 (1982) 13–26.
[47] M.A. Van der Hoef, R. Beetstra, J.A.M. Kuipers, Lattice-Boltzmann simulations of low-Reynolds-number flow past mono- and bidisperse arrays of spheres: results for the permeability and drag force, Journal of Fluid Mechanics 528 (2005) 233–254.
[48] S. Torquato, Random Heterogeneous Materials, Springer-Verlag, New York, 2002.
[49] D. Coelho, J.-F. Thovert, P.M. Adler, Geometrical and transport properties of random packings of spheres and aspherical particles, Physical Review E 55 (2) (1997) 1959.
[50] L. Lebon, L. Oger, J. Leblond, J.P. Hulin, N.S. Martys, L.M. Schwartz, Pulsed gradient NMR measurements and numerical simulation of flow velocity distribution in sphere packings, Physics of Fluids 8 (2) (1996) 293.
[51] B. Manz, L.F. Gladden, P.B. Warren, Flow and dispersion in porous media: lattice-Boltzmann and NMR studies, AIChE Journal 45 (9) (1999) 1845–1854.
[52] U. Tallarek, D. Kandhai, D. Hlushkou, A.G. Hoekstra, P.M.A. Sloot, H. Van As, Influence of stagnant zones on transient and asymptotic dispersion in macroscopically homogeneous porous media, Physical Review Letters 88 (23) (2002) 234501/1–234501/4.
[53] R.S. Maier, D.M. Kroll, R.S. Bernard, S.E. Howington, J.F. Peters, H.T. Davis, Pore-scale simulation of dispersion, Physics of Fluids 12 (2000) 2065.
[54] R.S. Maier, M.R. Schure, J.P. Gage, J.D. Seymour, Sensitivity of pore-scale dispersion to the construction of random bead packs, Water Resource Research 44 (2008), doi:10.1029/2006WR005577.
[55] U.M. Scheven, R. Harris, M.L. Johns, Intrinsic dispersivity of randomly packed monodisperse spheres, Physics Review Letters 99 (2007) 054502.